Role of Conserved Tyrosine Residues in NiSOD Catalysis: A Case of Convergent Evolution[†]

Robert W. Herbst,[‡] Abigail Guce,[‡] Peter A. Bryngelson,[‡] Khadine A. Higgins,[‡] Kelly C. Ryan,[‡] Diane E. Cabelli,[§] Scott C. Garman,*[,‡,||] and Michael J. Maroney*[,‡]

Department of Chemistry and Department of Biochemistry and Molecular Biology, University of Massachusetts, Amherst, Massachusetts 01003, and Department of Chemistry, Brookhaven National Laboratory, Upton, New York 11973

Received October 30, 2008; Revised Manuscript Received January 29, 2009

ABSTRACT: Superoxide dismutases rely on protein structural elements to adjust the redox potential of the metallocenter to an optimum value near 300 mV (vs NHE), to provide a source of protons for catalysis, and to control the access of anions to the active site. These aspects of the catalytic mechanism are examined herein for recombinant preparations of the nickel-dependent SOD (NiSOD) from *Streptomyces coelicolor* and for a series of mutants that affect a key tyrosine residue, Tyr9 (Y9F-, Y62F-, Y9F/Y62F-, and D3A-NiSOD). Structural aspects of the nickel sites are examined by a combination of EPR and X-ray absorption spectroscopies, and by single-crystal X-ray diffraction at ~1.9 Å resolution in the case of Y9F- and D3A-NiSODs. The functional effects of the mutations are examined by kinetic studies employing pulse radiolytic generation of O_2^- and by redox titrations. These studies reveal that although the structure of the nickel center in NiSOD is unique, the ligand environment is designed to optimize the redox potential at 290 mV and results in the oxidation of 50% of the nickel centers in the oxidized hexamer. Kinetic investigations show that all of the mutant proteins have considerable activity. In the case of Y9F-NiSOD, the enzyme exhibits saturation behavior that is not observed in wild-type (WT) NiSOD and suggests that release of peroxide is inhibited. The crystal structure of Y9F-NiSOD reveals an anion binding site that is occupied by either Cl^- or Br^- and is located close to but not within bonding distance of the nickel center. The structure of D3A-NiSOD reveals that in addition to affecting the interaction between subunits, this mutation repositions Tyr9 and leads to altered chemistry with peroxide. Comparisons with Mn(SOD) and Fe(SOD) reveal that although different strategies for adjusting the redox potential and supply of protons are employed, NiSOD has evolved a similar strategy for controlling the access of anions to the active site.

Superoxide dismutases (SODs)[1] are enzymes that catalyze the conversion of superoxide to molecular oxygen and hydrogen peroxide (eqs 4−3) and are thus part of cellular defenses against damage due to reactive oxygen species (ROS) (*1*−*4*).

$$M^{(n+1)} + O_2^{\bullet -} \rightarrow M^{(n)} + O_2 \quad (1)$$

$$M^{(n)} + 2H^+ + O_2^{\bullet -} \rightarrow M^{(n+1)} + H_2O_2 \quad (2)$$

$$2O_2^{\bullet -} + 2H^+ \rightarrow O_2 + H_2O_2 \quad (3)$$

SODs utilize one-electron redox-active metal centers to carry out catalysis. There are four known SODs categorized by the metal present: (1) Cu/Zn, (2) Mn, (3) Fe, and (4) Ni. These four SODs fall into three protein classes based on amino acid sequence homology, with Fe and Mn in the same class. In addition to having no sequence homology with other SODs (*5*), NiSOD has other notable differences. Nickel is the only metal found in a SOD where the aquated ion does not react with O_2^- (*1*), presumably because the redox potential of $Ni(OH_2)_6^{2+/3+}$ (>2 V) (*6*) lies outside of the potentials for oxidation and reduction of O_2^-. In SODs, the protein component serves at least three important functions with regard to catalysis: to adjust the redox potential of the metallocenter (*7*−*10*), to provide a source of protons (*11, 12*), and to control the access of anions to the active site (*13*−*16*). In NiSOD, the mechanism by which the protein tunes the redox potential of nickel is also distinct from those of other SODs in that it is the only metal center that employs cysteine

[†] This work was supported by National Science Foundation Grants MCB-0321482 and CHE-0809188 to M.J.M. S.C.G. acknowledges the University of Massachusetts and the Charles H. Hood Foundation for support. The U.S. Department of Energy, Division of Materials Sciences and Division of Chemical Sciences, supported XAS and X-ray diffraction data collection at the National Synchrotron Light Source (NSLS) at Brookhaven National Laboratory. The National Institutes of Health supports beamlines X3B and X6A at NSLS. Pulse radiolysis studies were funded under Contract DE-AC02-98CH10886 with the U.S. Department of Energy.

* To whom correspondence should be addressed. Phone: (413) 545-4876. Fax: (413) 545-4490. E-mail: mmaroney@chemistry.umass.edu.

[‡] Department of Chemistry, University of Massachusetts.

[§] Brookhaven National Laboratory.

[||] Department of Biochemistry and Molecular Biology, University of Massachusetts.

[1] Abbreviations: SOD, superoxide dismutase; XAS, X-ray absorption spectroscopy; EPR, electron paramagnetic resonance; NHE, normal hydrogen electrode; ROS, reactive oxygen species; PDTC, bis[pyridine-2,6-bis(thiocarboxylate)]nickel(III); EXAFS, extended X-ray absorption spectroscopy; XANES, X-ray absorption near edge structure; ICP-OES, inductively coupled plasma optical emission spectroscopy; ESI-MS, electrospray ionization mass spectrometry; DSC, differential scanning calorimetry; Amp, ampicillin; Cam, chloramphenicol; OD, optical density; FPLC, fast protein liquid chromatography; IPTG, isopropyl β-D-1-thiogalactopyranoside; PDB, Protein Data Bank; PCR, polymerase chain reaction.

10.1021/bi802029t CCC: $40.75
Published on Web 01/30/2009

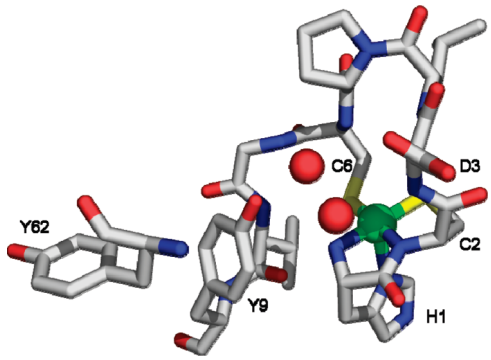

FIGURE 1: Active site from one monomer of the homohexameric NiSOD from *S. coelicolor*, showing the first nine residues and Tyr62 (*17*). The nickel is shown in the five-coordinate pyramidal oxidized His-on form. PDB entry 1T6U. The image was generated with PyMOL (*75*).

thiolate ligands (*17*−*21*), which at first glance would seem to be incompatible with a catalytic center that produces oxygen and peroxide (*22*−*24*).

Crystal structures of NiSOD reveal a five-coordinate pyramidal site that is associated with an oxidized Ni(III) center (Figure 1), and a four-coordinate planar site associated with a reduced Ni(II) center (*17, 21*). The nickel ligands derive from three amino acid residues: the N-terminal amino group of His1, an amidate N-donor from Cys2, and side chain thiolates from Cys2 and Cys6. The fifth ligand in the Ni(III) site is provided by the imidazole side chain of His1 (His-on), which is unbound in the Ni(II) (His-off) site (*17, 21*).

There are four tyrosine residues in the amino acid sequence of *Streptomyces coelicolor* NiSOD, two of which (Tyr9 and Tyr62) are conserved in nearly all NiSODs (see the Supporting Information). Tyr9 is positioned near the vacant coordination site opposite the His1 imidazole ligand in the His-on structure (O−Ni distance of 5.47 Å) and is involved in H-bonding with two ordered water molecules in the active site, neither of which is a nickel ligand (O−Ni distances of 2.57 and 3.15 Å). These water molecules are also H-bonded to amide protons from Cys6 and Asp3. The other conserved tyrosine, Tyr62, is near Tyr9 and ∼13 Å from the nickel center.

The SOD proteins supply protons for the production of H_2O_2 and control access of anions to the active sites (*7*−*10*). NiSOD lacks an aqua ligand that has been associated with redox tuning and proton supply (*8*) in MnSOD and FeSOD, but the thiolate ligands may serve an analogous role (*25, 26*). Anion access is controlled in SODs using a combination of size constraint (*27*), electrostatic steering (*28*−*30*), and, in the cases of MnSOD (*12, 31, 32*) and FeSOD (*15, 33*), a "gatekeeper" tyrosine and neighboring phenylalanine (*27*). Herein, we probe the role of the conserved tyrosine residues and the aspartate (Asp3) in the Ni hook domain for insights into the NiSOD mechanism using a combination of mutagenesis to systematically perturb the tyrosine residues, crystallographic and spectroscopic studies to assess the structural ramifications of the mutations, and kinetics using pulse radiolytic generation of superoxide to examine function. The mutation of Tyr9 led to the serendipitous isolation and the first crystallographic characterization of an anion complex of NiSOD (Cl^- and Br^-). In addition to intersubunit interactions, Asp3 also affects the position of Tyr9 in a way that changes the function of the active site. The results point to a role for Tyr9 in the mechanism for regulating anion access that has many features in common with other SODs, particularly MnSOD. Thus, NiSOD represents a fascinating case of molecular convergent evolution.

EXPERIMENTAL PROCEDURES

Molecular Biological Methods. The *sodN* gene from H15 (the native gene has a 14-amino acid leader sequence that is cleaved in vivo, leaving H15 as the first amino acid after post-translation modification) forward was cloned out of the pET3a-SODN vector using PCR amplification with the primers 5′-GGTATTGAGGGTCGCCACTGCGACCTGCCCTG-3′ (5′SODN15) and 5′-AGAGGAGAGTTAGAGCCCTTTGTTAGCAGCCGG-3′ (3′SODNU). The PCR product was purified from a 1% agarose gel. Treatment of the PCR product with T4 DNA polymerase created overhangs complementary to ligation independent cloning (LIC) vector pET30 Xa/LIC (Novagen). The *sodN* gene was annealed into the vector directly after the factor Xa recognition site (IEGR) so that upon cleavage with factor Xa, H1 would be the N-terminal residue. This 47-amino acid N-terminal extension also contains a His tag used during purification to isolate the fusion peptide (vide infra). The insert was annealed to the vector, and NovaBlue (Novagen) competent cells were transformed with the pET30 Xa/LIC plasmid containing the *sodN* gene. The NovaBlue cells were plated on LB medium containing 34 μg/mL kanamycin (kan) and grown overnight at 37 °C. Plasmid mini preps (Qiagen) were performed after single colonies were grown in 3 mL of LB kan medium overnight. BL21(DE3) pLysS (Novagen) competent cells were transformed with plasmid pET-30Xa/LIC-SODNH15 (pSODNH15) and were plated and grown overnight at 37 °C on LB medium containing kan and 30 μg/mL chloramphenicol (cam). Single colonies were grown overnight in 3 mL cultures (LB kan/cam) and diluted 1:100 in 100 mL of fresh medium. Cells were grown at 37 °C to an OD at 600 nm of 0.6 and induced with isopropyl β-D-thiogalactoside (IPTG), at a final concentration of 0.8 mM. After 3 h, the cells were harvested via centrifugation, and SDS−PAGE was conducted on cell extract to determine expression of the target fusion protein. Plasmids producing proteins of the appropriate molecular mass (18 kDa) were submitted to the University of Massachusetts DNA sequencing facility to confirm the presence of the His-tagged wild-type (WT) gene.

Single colonies of cells containing the pSODNH15 plasmid were grown in a 10 mL culture (LB cam/kan) overnight at 37 °C with shaking and then added to 1 L of prewarmed fresh medium. Cultures were grown to an OD at 600 nm of 0.6 and induced (0.8 mM IPTG) for 3 h. Cells were harvested by centrifugation, resuspended in 50 mL of Ni-NTA binding buffer [10 mM imidazole, 50 mM sodium phosphate, and 300 mM sodium chloride (pH 8.0)] with 1 mM phenylmethanesulfonyl fluoride (PMSF), and frozen at −80 °C. Cells were thawed, and 100 μL of a DNase I solution [10 mg/mL DNase I, 10 mM magnesium chloride, 20 mM Tris (pH 7.5), and 40% glycerol] was added and the mixture incubated at 37 °C until the viscosity of the solution was significantly reduced. All chromatographic purifications employed an AKTA-FPLC system (Amersham Biosciences). The cell lysate was then loaded onto a column (Pharmacia HR10) containing Ni-NTA His·Bind Superflow resin

Table 1: Mutagenic Primers for Y62F- and Y9F/Y62F-NiSOD

mutant	forward primer	reverse primer	parental DNA
Y62F-NiSOD	5′-GCTGTGGAGCGAC**TTC**TTCAAGCCCCCGC-3′	5′-GCGGGGGCTTGAAG**AAG**TCGCTCCACAGC-3′	WT-NiSOD
Y9F/Y62F-NiSOD	5′-GCTGTGGAGCGAC**TTC**TTCAAGCCCCCGC-3′	5′-GCGGGGGCTTGAAG**AAG**TCGCTCCACAGC-3′	Y9F-NiSOD

(Novagen). Nonspecifically or weakly bound proteins were removed by using a step gradient of 0 to 30% elute buffer [250 mM imidazole, 50 mM sodium phosphate, and 300 mM sodium chloride (pH 8.0)]. Following a wash step, the fusion protein was eluted from the column with 100% elute buffer. The eluted protein was then dialyzed into factor Xa buffer [5 mM calcium chloride, 50 mM Tris, and 100 mM sodium chloride (pH 8.0)] that contained 0.25 mM PMSF to prepare the sample for N-terminal processing.

N-Terminal processing (required to remove the leader sequence, which contains the His tag for purification) was accomplished by cleaving the fusion protein at the IEGR site using factor Xa. The cleavage reaction was performed at 4 °C until the reaction was complete, as monitored by SDS−PAGE. Subsequently, the reaction mixture was dialyzed against 20 mM Tris-HCl (pH 8.0) to remove excess salt. Anion exchange chromatography (Pharmacia FPLC-Mono Q) using a 350 mM sodium chloride gradient over 10 column volumes at a slow flow rate of 0.5 mL/min gave pure apo-NiSOD in the first fractions off the column, as confirmed by the molecular weights of the products obtained from ESI-MS (Table 3) and by Edman N-terminal peptide sequencing (Midwest Analytical, Inc., St. Louis, MO). The oligomeric state of the protein (hexamer) was confirmed by size-exclusion chromatography and by ESI-MS under nondenaturing conditions (Supporting Information, vide infra).

Reconstitution of the recombinant, N-terminally processed apo-NiSOD was achieved by addition of a 3-fold excess of dithiothreitol (DTT) for 2 h in an anaerobic chamber (Coy Laboratory Products Inc., Grass Lakes, MI) followed by addition of a 5-fold excess of $NiCl_2$. The properties of the reconstituted enzyme were virtually identical to those previously reported for native enzymes (see Results).

D3A-NiSOD. The mutation of Asp3 to Ala was made by PCR. The PCR used the WT-NiSOD gene along with 3′SODNU and the mutagenesis primer 5′-GGTATTGAGGGTCGCCACTGC**GCG**CTGCCCTGCGGCG-3′. The PCR product was gel purified (2% agarose), and the gene was ligated into the pET30 Xa/LIC vector and then transformed, overexpressed, purified, processed, and reconstituted with nickel chloride ($NiCl_2$) in the same manner as WT-NiSOD (vide supra).

To probe the nature of a protein-based radical signal observed in the product of the reaction of D3A-NiSOD with H_2O_2, a sample of this mutant in which all four tyrosine residues present were substituted with d_4-Tyr was prepared. Thus, all four aromatic protons are substituted with deuterons in each Tyr residue. To incorporate d_4-Tyr into D3A-NiSOD, *Escherichia coli* BL21(DE3) pLysS cells were grown in LB broth until they reached an OD at 600 nm of 0.6. The cells were then spun down and resuspended in M9 medium containing glyphosate (1 g/L), Trp, His, Phe, and d_4-Tyr (0.5 g/L) and grown for an additional 30 min before being induced with 1 mL of IPTG (200 mg/mL). Cells were grown for an additional 3 h and then harvested. d_4-Tyr-D3A-NiSOD was purified and isolated as described above for WT-NiSOD.

Y9F-NiSOD. The Y9F point mutation was introduced in two steps. Two fragments were created in two different PCRs (reactions A and B) using the WT gene. Reaction A utilized the 5′SODN15 primer and 5′-GCGGCGTG**TTC**GACCCTGCCCAG-3′, while reaction B used the 3′SODNU primer along with 5′-GGCCGTCCAGGAGAAGCTGGCCGGCAACGACGACG-3′. The PCR fragments were gel purified (2% agarose) and then combined with the 5′SODN15 and 3′SODNU primers in a third PCR to generate the NiSOD gene with Tyr9 mutated to a Phe. The mutated gene was ligated into the pET30 Xa/LIC vector as described for WT-NiSOD (vide supra). The transformation, overexpression, isolation, purification, and N-terminal processing of Y9F-NiSOD were performed in the same manner described for WT-NiSOD (vide supra).

Y62F- and Y9F/Y62F-NiSOD. Both Y62F- and Y9F/Y62F-NiSOD were made using the QuikChange (Stratagene) mutagenesis kit. Table 1 shows the primers and the parental DNA that were used in the two PCRs. DNA isolated using the Qiagen miniprep kit was sequenced at the W. M. Keck DNA facility (Yale University, New Haven, CT) to ensure that the correct mutation was present. Transformation, induction, protein purification, and N-terminal processing were preformed as described above for WT-NiSOD. The protein product was confirmed by the molecular weight of the fusion protein determined using ESI-MS (Table 3, vide infra).

Quaternary Structure and Stability. The oligomeric states as well as the stabilities of WT and mutant NiSODs were determined by a combination of three techniques: size-exclusion chromatography, ESI-MS under nondenaturing conditions, and differential scanning calorimetry (DSC). Size-exclusion chromatography employed solutions of WT-NiSOD or mutant NiSODs that were applied to a HiLoad 16/60 Superdex 200 (GE lifesciences) column. The column was standardized with albumin (67 kDa), ovalbumin (43 kDa), chymotrypsinogen (25 kDa), and ribonuclease A (13.7 kDa). All reconstituted NiSOD samples eluted with molecular weights appropriate for homohexamers. To determine the MW of the expression products, ESI-MS was performed using a Bruker Esquire mass spectrometer on solutions of denatured proteins in an aqueous ammonium acetate solution (final concentration of 5 mM) with 3% acetic acid and 50% MeOH. To confirm the oligomeric state of the enzyme, ESI-MS was also performed on a JMS-700 MStation magnetic sector (double focusing) mass spectrometer under "nondenaturing conditions". To prevent oligomeric breakdown, the orifice voltage was turned to 0 V and the skimmer voltage was set to 120 V. A solution of 60 μM NiSOD monomer dissolved in 10 mM ammonium acetate solution was used. Under these conditions, WT-NiSOD exhibits peaks characteristic of the hexameric holoprotein and little else (see the Supporting Information).

Differential scanning calorimetry thermograms were measured with a Microcal VP-DSC with 0.5 mL of sample and reference cells. NiSOD samples were concentrated to 2−5

Table 2: NiSOD Mutant Data Collection and Refinement Statistics

	in house	synchrotron		
NiSOD mutant	Y9F (Cl) [3G4X][a]	Y9F (Cl) [3G4Z]	Y9F (Br)	D3A [3G50]
		Data Collection		
wavelength (Å)	1.5418		0.9184	
resolution (last shell) (Å)	50−2.01 (50−2.02)	20.9−1.87 (1.94−1.87)	(1.94−1.87)	21.57−1.90 (1.97−1.90)
cell parameters ($C222_1$) *a*, *b*, *c* (Å)	60.09, 112.57, 111.87	59.87, 111.58, 111.55	59.99, 112.46, 110.96	59.99, 112.27, 111.70
no. of observations	118668	211352	127478	238695
no. of unique observations (last shell)	25413 (2175)	29628 (2765)	29651 (2757)	29881 (2929)
multiplicity (last shell)	4.7 (4.4)	7.1 (5.7)	4.3 (3.2)	8.0 (7.2)
completeness (%) (last shell)	99.4 (97.8)	95.3 (91.0)	94.2 (89.1)	99.9 (99.9)
R_{sym} (last shell)	0.054 (0.515)	0.030 (0.337)	0.038 (0.732)	0.046 (0.929)
I/σ_I (last shell)	28.0 (3.1)	42.1 (3.0)	28.5 (1.6)	41.6 (2.3)
		Refinement		
R_{work}/R_{free} (%)	16.8/23.7	18.3/25.4		18.6/24.0
average *B*-factor (Å^2)	26.8	30.7		38.0
no. of atoms	3213	3249		3058
no. of waters	389	458		291

[a] PDB codes listed in [].

Table 3: Analytical Data for WT-NiSOD and Its Mutants

NiSOD sample	ESI-MS MW[a] (calcd value)	quaternary structure[d]	no. of Ni atoms per protein	EPR as isolated [% Ni(III)]	kinetics,[e] $k_{calc} \times 10^8$ M^{-1} s^{-1} at pH 7.5 [range of O_2^- concentrations (μM)]	$E_{1/2}$ (mV vs NHE) reductive titration	$E_{1/2}$ (mV vs NHE) oxidative titration	T_m (°C)
WT	18171.2[b] (18169.6)	hexamer	0.88	g = 2.30, 2.23, 2.01; A_{zz} = 24.9 G [51(2)]	7.07 (1.93−5.97)	290(4)	279(6)	84.8
D3A	13160.9[c] (13157.0)	hexamer with decreased stability	1.11	g = 2.30, 2.24, 2.01; A_{zz} = 24.9 G [48(2)]	2.09 (1.68−5.99)	308(3)	290(7)	73.9
Y9F	13183.4[c] (13185.0)	hexamer	0.72	g = 2.30, 2.23, 2.01; A_{zz} = 24.9 G [53(2)]	3.71 (1.54−2.38)	297(5)	299(8)	86.3
Y62F	18154.1[b] (18153.3)	hexamer	0.90	g = 2.30, 2.23, 2.01; A_{zz} = 24.9 G [48(2)]	6.42 (2.09−9.8])	ND	ND	82.4
Y9F Y62F	18137.5[b] (18137.2)	hexamer	0.74	g = 2.30, 2.23, 2.01; A_{zz} = 24.4 G [46(2)]	2.41 (2.18−4.12)	ND	ND	74.7

[a] ESI-MS measurements were conducted under denaturing conditions resulting in monomer MW values of processed NiSOD or fusion peptide. [b] Fusion peptide. [c] Processed NiSOD. [d] From size-exclusion chromatography and/or ESI-MS under nondenaturing conditions (see Experimenta Procedures). [e] Rates determined under first-order conditions; $k_{calc} = k_{obs}$/[Ni], where [Ni] = 2 μM. The value of k_{calc} was determined by averaging the values over the range of O_2^- concentrations where there is no apparent decrease in k_{obs}.

Table 4: XANES Analysis of Dithionite-Reduced WT-NiSOD and Mutant Enzymes

sample	edge energy (eV)	1s → 3d peak area ($\times 10^{-2}$ eV)	geometry	ref
WT	8340.5(2)	4.7(5)	planar, CN = 4	*47*
Y9F	8339.5(2)	5(2)	planar, CN = 4	this work
Y62F	8339.3(2)	3.2(4)	planar, CN = 4	this work
Y9F/Y62F	8340.0(2)	5.8(5)	SPY, CN = 5	this work
D3A	8342.0(2)	4.5(5)	planar, CN = 4	this work

μM hexamer (Y62F- and Y9F/Y62F-NiSOD) or 100−140 μM in hexamer (WT-, D3A-, Y9F-NiSOD) in buffer [50 mM Tris-HCl (pH 8.0)], degassed under vacuum, and added via syringe to the sample and reference cells. Spectra were collected at 30 psi between 6 and 100 °C at a scan rate of 30 °C/h. Baseline correction and normalization were performed with the Microcal interface to the Origin graphing program. Peak maxima were taken as melting temperatures, T_m. The values of T_m obtained are listed in Table 3, and thermograms are included as Supporting Information.

Electron Paramagnetic Resonance (EPR). X-Band EPR spectra were recorded on a Bruker ELEXSYS E-500 X-band spectrometer. Samples in polycarbonate XAS holders were inserted into a liquid N_2 finger dewar. The data were collected over a 1000 G field centered at 3000 G. The modulation receiver and signal-channel parameters were as follows: modulation frequency of 100 kHz, modulation amplitude of 10 G, and time constant of 327 ms. The microwave power was set to 20 mW with a frequency of 9.46 GHz. To determine the number of Ni(III) centers present in each mutant NiSOD, spin integration was performed on each EPR spectrum. The concentration of Ni in each sample was determined using ICP-OES (λ = 231.604 nm) on a Perkin-Elmer Optima 4300 DV instrument. The resulting EPR spectra were then integrated twice and compared to a spin standard with a known concentration, bis[pyridine-2,6-bis(thiocarboxylate)]nickel(III) (NiPDTC) (*34*), to determine the percentage of Ni centers that were in the oxidized state (Table 3).

Redox Titrations. A modification of the procedure of Reiter et al. was used to determine the $E_{1/2}$ values of WT-NiSOD and the various mutants (*35*). Solutions of NiSOD (3 mL, 100−200 μM) were prepared in 100 mM potassium phosphate buffer (pH 7.5) with 100 mM potassium chloride as a supporting electrolyte. Samples were degassed and kept under argon throughout the experiment. Electrochemical potentials were monitored with an Extech Instruments True rms digital multimeter connected to a platinum wire and a Ag/AgCl reference electrode. Optical spectra were monitored on a Hewlett-Packard 8452A diode array spectrophotometer equipped with a thermostated cell holder that held all samples at 25 °C.

Prior to the experiment, the samples were treated with $KMnO_4$ (3 μL aliquots of a 6 mM aqueous solution) until the absorbance at 380 nm was at a maximum, ensuring the

enzyme was in its most oxidized form. Reductive titrations were performed by adding aliquots (1−5 μL) of reduced methylviologen [6 mM, electrochemically prepared with a Bioanalytical Systems (BAS) CV50W instrument using a BAS bulk electrolysis cell under argon; concentration was confirmed by measuring the absorption of the MV^+ solution at 606 nm, $\varepsilon = 13700\ cm^{-1}\ M^{-1}$ (*36*)] via a Hamilton gastight syringe. After complete reduction, the oxidative titrations were performed in a similar manner by the addition of small aliquots (1−5 μL) from a 6 mM $KMnO_4$ stock solution (degassed).

The data were plotted as absorbance (at 378 nm) versus potential (converted to NHE) and fit to eq 4, which was derived from the Nernst equation by the method of Bernhardt et al. (*37*)

$$\text{absorbance} = \frac{A_{ox} \times 10^{n(E-E\circ)/59} + A_{red}}{1 + 10^{n(E-E\circ)/59}} \quad (4)$$

where A_{ox} is the absorbance of the solution when all the species are in the oxidized form, A_{red} is the absorbance of the solution when all the species are present in the reduced form, n is the number of electrons being transferred during the reaction, and $E°$ is the midpoint potential of the redox reaction. To obtain the reported $E°$ values for NiSOD samples, n was fixed at 1.0 and the other three parameters were allowed to vary.

X-ray Absorption Spectroscopy. X-ray absorption spectroscopy (XAS) data collection and analysis were performed as previously described (*38*). Ni *K*-edge XAS data were collected on beamline X9B at the National Synchrotron Light Source (Brookhaven National Laboratory). Samples of frozen protein solutions [1−3 mM, based on Ni content, in 20 mM Tris-HCl (pH 8.0)] were placed in polycarbonate holders inserted into aluminum blocks and held near 50 K using a He displex cryostat. The ring conditions for data collection were 2.8 GeV and 120−300 mA. A sagittally focusing Si(111) double-crystal monochromator and a 13-channel Ge fluorescence detector (Canberra) were used for data collection. X-ray absorption near-edge spectroscopy (XANES) data was collected from −200 to 200 eV relative to the Ni edge. The edge energy reported was taken to be the maximum of the first derivative of the XANES spectrum. Extended X-ray absorption fine structure (EXAFS) was collected to 9307 eV ($k = 16\ Å^{-1}$). The X-ray energy for the K-edge of Ni was internally calibrated to 8331.6 eV using transmission data from a Ni foil. The data shown are the average of four to eight scans and were analyzed using EXAFS123 for XANES data (*39*), and SixPack was used for EXAFS analysis (*40*). Scattering parameters for EXAFS fitting were generated using FEFF 8 (*41*). SixPack builds on the ifeffit engine (*41, 42*) and uses iterative FEFF calculations to fit EXAFS data during model refinement and is thus an improvement over previous methods that employ a static set of calculated scattering parameters. To compare different models to the same data set, ifeffit uses three goodness of fit parameters, χ^2, reduced χ^2, and the *R*-factor. χ^2 is given by eq 5

$$\chi^2 = \frac{N_{idp}}{N_{\varepsilon^2}} \sum_{i=1}^{N} \{[\text{Re}(f_i)]^2 + [\text{Im}(f_i)]^2\} \quad (5)$$

where N_{idp} is the number of independent data points, N_{ε^2} is the number of uncertainties to minimize, $\text{Re}(f_i)$ is the real part of the EXAFS fitting function, and $\text{Im}(f_i)$ is the imaginary part of the EXAFS fitting function. Reduced $\chi^2 = \chi^2/(N_{ind} - N_{varys})$ (where N_{varys} is the the number of refining parameters) and represents the degrees of freedom in the fit. Ifeffit also calculates the *R*-factor for the fit, which is given by eq 6 and is scaled to the magnitude of the data, making it proportional to χ^2.

$$R = \frac{\sum_{i=1}^{N} \{[\text{Re}(f_i)]^2 + [\text{Im}(f_i)]^2\}}{\sum_{i=1}^{N} \{[\text{Re}(\tilde{x}\text{data}_i)]^2 + [\text{Im}(\tilde{x}\text{data}_i)]^2\}} \quad (6)$$

To compare different models (fits), the *R*-factor and reduced χ^2 parameters can be assessed to determine which model is the best fit, in which case both parameters should be minimized. Although the *R*-factor will always improve with an increasing number of adjustable parameters, reduced χ^2 will go through a minimum and then increase, indicating that the model is over fitting the data.

Crystallography. Crystallization experiments were performed using the hanging-drop vapor-diffusion method. All crystals grew after 2−3 weeks at 20 °C. Crystals of Y9F-NiSOD (Cl) were obtained by mixing 1 μL of the reservoir solution [0.05 M $CaCl_2$, 0.1 M Bis-Tris (pH 6.5 with HCl), and 25% (v/v) PEG MME (Fluka) 550] with 1 μL of a protein solution at 8.0 mg/mL in a buffer of 50 mM Tris-HCl (pH 8.0). Prior to being frozen and data collection, the crystals were transferred stepwise into a cryoprotectant solution containing 40% (v/v) PEG MME (Fluka) 550, 0.05 M $CaCl_2$, and 0.1 M Bis-Tris (pH 6.5 with HCl).

To produce crystals of Y9F-NiSOD (Br) with bromide in place of chloride, the protein was exchanged into a buffer solution containing 50 mM Tris-HBr (pH 8.0). Crystals of Y9F-NiSOD (Br) were obtained by mixing 1 μL of the reservoir solution [0.1 M Bis-Tris (pH 6.5 with HBr) and 30% (v/v) PEG MME (Fluka) 550] with 1 μL of a protein solution at 8.0 mg/mL. Prior to being frozen and data collection, the crystals were transferred stepwise into a cryoprotectant solution containing 40% (v/v) PEG MME (Fluka) 550 and 0.1 M Bis-Tris (pH 6.5 with HBr).

Crystals of D3A-NiSOD were obtained by mixing 1 μL of the reservoir solution [0.05 M $MgCl_2$, 0.1 M HEPES (pH 7.5), and 30% (v/v) PEG MME (Fluka) 550] with 1 μL of a protein solution at 8.2 mg/mL in 50 mM Tris-HCl (pH 8.0). Prior to being frozen and data collection, the crystals were transferred stepwise into a final cryoprotectant solution containing 40% (v/v) PEG MME (Fluka) 550, 0.5 M $MgCl_2$, and 0.1 M Bis-Tris (pH 6.5).

Crystals were frozen in liquid nitrogen and then transferred into a gaseous nitrogen stream at 100 K for X-ray data collection. Data collection was performed at National Synchrotron Light Source (NSLS) beamline X6A at the Brookhaven National Laboratory. All data were collected at 13500 eV (0.9184 Å), which is above the Br absorption edge energy. Each frame consisted of 0.75° rotation taken for exposures of 5 s [for Y9F (Cl^-) and Y9F (Br^-)] or 15 s (for D3A). X-ray images were integrated, indexed, and scaled using HKL2000 (*43*). The diffraction data were scaled in space group $C222_1$, leading to a solvent content of 47% and

three subunits in the asymmetric unit. Data collection and refinement statistics are given in Table 2.

Molecular replacement calculations were performed in the CCP4 program MolRep (*44*) using a trimeric search model derived from the native NiSOD structure (PDB entry 1T6Q) (*1*). The starting model for manual building was the native structure with the first 10 amino acids and the solvent molecules omitted. Rigid body refinement and positional refinement with 3-fold noncrystallographic symmetry (NCS) imposed were performed using the CCP4 program Refmac5 (*44*), and $2F_o - F_c$ and $F_o - F_c$ electron density maps showed substantial density representing the omitted parts of the model. The entire model, including the 10 N-terminal amino acids, was built into the electron density using the O graphics program (*45*). Weighted $2F_o - F_c$ and $F_o - F_c$ maps were examined at each stage of the refinement. In later rounds of refinement, heteroatoms, such as the $Ni^{2+/3+}$, Cl^-, and Br^- ions, were assigned to electron density peaks. The experimental electron density was of very high quality except for that of the seven N-terminal residues, where 3-fold averaging was imposed to aid in map interpretation. The final statistics for the model are presented in Table 2. To determine if the electron density near the Ni in the Y9F-NiSOD structure was Cl^- or water, crystals were grown using Br^- instead of Cl^-. After the determination that the Cl^- was replaced with Br^-, the Y9F (Br) structure was not fully refined because the Y9F (Cl) data were of better quality. The quality of the model was assessed with PROCHECK (*46*).

Kinetics. The kinetics of superoxide dismutation was examined using pulse radiolytic generation of superoxide and was carried out at Brookhaven National Laboratory as previously described (*47*). Samples of NiSOD (final concentration of 2 μM, based on the Ni concentration) were placed into a 2 cm cuvette that contained phosphate buffer (10 mM), formate (30 mM), and ethylenediaminetetraacetic acid (EDTA, 5 μM). The sample was then pulsed from a 2.0 MeV van de Graaff accelerator, varying the pulse width (100−2000 ns), resulting in a range of initial superoxide concentrations (2−40 μM). The disappearance of the absorbance at 260 nm that corresponds to O_2^- was fit to a first-order process (Figure 7 of the Supporting Information). Catalytic rate constants were determined by dividing the first-order rate by the nickel concentration, assuming all of the nickel is bound and active in the enzyme. The rate of O_2^- disappearance in the absence of NiSOD was measured for the O_2^- concentrations and pHs used and was, in all cases, at least 1 order of magnitude slower than the enzymatically driven rate. The rate constants are reported on a per Ni basis as determined by the Ni content of each sample. Nickel content was determined by ICP-OES using the Ni wavelength of 231.604 nm.

Reactions with H_2O_2. Both WT- and D3A-NiSOD in 20 mM Tris-HCl (pH 8) were treated anaerobically with a 10-fold excess of H_2O_2 at room temperature. The peroxide concentration was determined by titration with a standard solution of potassium permanganate (*48*). After 10 min, the peroxide was buffer exchanged using spin concentrators (Vivaspin, 5K MW cutoff) and five 1:10 dilutions with buffer. The resulting enzyme solutions were examined by pulse radiolysis to determine if any activity was lost. A portion of each solution was set aside for MW determination by ESI-MS to determine if oxygen incorporation had occurred.

RESULTS

Protein Characterization. Data regarding the molecular weight of expressed protein, the quaternary structure, the T_m, and the Ni content following reconstitution of recombinant proteins are summarized in Table 3. All of the recombinant proteins had the MW expected for the amino acid substitutions involved, and all were present largely as homohexamers following reconstitution with $NiCl_2$. In the case of D3A-NiSOD, a significant amount of monomeric protein was also observed in the nondenaturing mass spectrum (see the Supporting Information); however, this was not observed by size-exclusion chromatography, indicating that the protein is not completely stable to the ESI-MS conditions. These results are consistent with the lower T_m value obtained from DSC analysis (Table 3). WT and Y9F had high thermal stabilities with T_m values of 84.8 and 86.3 °C, respectively, whereas D3A had a lower thermal stability (T_m = 73.9 °C), which may be attributed to weaker interactions between subunits in the hexamer (vide infra).

Electron Paramagnetic Resonance. EPR spectroscopy was used to examine the redox state of the nickel center in the resting enzymes and probe the electronic structure of the Ni(III) site in mutant NiSODs. The EPR data show that the Ni(III) center present in all the mutants is similar to that of WT-NiSOD. As isolated, native NiSOD has a distinctive rhombic EPR spectrum that arises from a five-coordinate, low-spin, $S = {}^1/_2$ Ni(III) center, with the unpaired electron in d_{z^2}. X-Band EPR spectra of the WT recombinant NiSOD, tyrosine mutants (Y9F, Y62F, and Y9F/Y62F) and D3A (Table 3) also exhibit typical rhombic Ni(III) signals with strong N-hyperfine splittings on the g_z feature (A_z = 24.9 G) arising from the apical imidazole bound to the Ni(III) center (*47, 49*). The electronic structure of the Ni(III) center was not expected to be greatly perturbed by mutations in the second coordination sphere, and this was confirmed by the spectra obtained (Table 3). When Tyr9 is mutated to Phe, subtle hyperfine structure on the g_y feature that is not resolved in the spectrum of WT-NiSOD is observed (Supporting Information).

Careful integration of the Ni(III) signal in WT-NiSOD indicates that the EPR signal accounts for only half of the nickel present in the samples (Table 3). All samples were approximately 50:50 Ni(III):Ni(II). Excess potassium permanganate or hexachloroiridate was used in attempts to oxidize the remaining Ni(II) centers in as-isolated WT-NiSOD. In both cases, no additional oxidation was seen. These results do not coincide with a previous report in which excess ferricyanide was used to reach a maximum level of oxidation of 72% Ni(III) in WT-NiSO (*17*). However, it should be noted that both permanganate and hexachloroiridate are stronger oxidants than ferricyanide, which has a redox potential (360 mV) that is barely above the midpoint potential of the enzyme.

In summary, the EPR results from the nickel center are consistent with a resting oxidized state that contains 50% Ni(III) and 50% Ni(II), which is not significantly perturbed by mutation of Tyr9 or Asp3.

Table 5: EXAFS Analysis for Dithionite-Reduced NiSOD Samples

sample	N	*R* (Å)	σ^2 ($\times 10^3$ Å^{-2})	$\Delta E°$ (eV)	reduced χ^2	*R*-factor
WT[a]	2N	1.91(1)	1(2)	−3.4	N/A	0.64[c]
	2S	2.160(4)	0(4)	−3.2		
WT[b]	2N	1.83(4)	10(4)	−17(3)	22.8	0.11
	2S	2.16(2)	7(1)			
	2C	2.73(4)	3(5)			
	2C	2.90(5)				
Y9F	2N	1.95(2)	5(2)	−7(2)	22.2	0.06
	1S	2.23(2)	3(1)			
	1S	2.52(3)	6(4)			
	2C	3.00(4)	4(4)			
Y62F	1N	1.90(3)	5(4)	−10(2)	11.2	0.04
	1N	2.2(2)				
	2S	2.17(3)	5(2)			
	3C	2.85(3)	2(2)			
	2C	3.03(4)				
D3A	3N	2.08(2)	2.3(9)	−7(1)	9.04	0.04
	2S	2.13(1)	8(3)			
	2C	2.95(6)	12(8)			
Y9F/Y62F	2N	2.02(6)	12(6)	−5(3)	14.7	0.09
	1S	2.20(2)	2(1)			
	1S	2.46(4)	6(3)			
	2C	3.02(5)	6(6)			

[a] WT reduced NiSOD from ref *48*. [b] WT reduced NiSOD from this work and fit using SixPack. [c] GOF parameter calculated by EXAFS123 (*39*).

X-ray Absorption Spectroscopy. XAS studies were used to confirm that the nickel center was bound to the correct protein site in the reconstituted WT protein and to characterize the nickel site in the mutant NiSODs, as well as to supplement the results of the crystallographic investigations of the nickel sites in Y9F-NiSOD and D3A-NiSOD and allow comparisons with other mutants. Since the oxidized enzymes always contain a mixture of oxidized and reduced nickel centers, the samples studied were all reduced with sodium dithionite prior to XAS data collection and were EPR silent. The results for the XAS experiments on the tyrosine mutants of NiSOD are summarized in Tables 4 and Tables 5 and Figure 2.

XANES. XANES (X-ray absorption near edge structure) yields information about the coordination number and geometry of the nickel site. Nickel has vacancies in the 3d manifold, which give rise to transitions in the XANES region of the XAS spectrum that are dependent on the geometry and coordination number of the metal site. These transitions include the 1s → 3d and 1s → $4p_z$ (plus shakedown contributions), which occur near 8331 and 8336 eV, respectively, in Ni(II) complexes (*50*). In WT-NiSOD and in the mutant NiSODs, both transitions are observed, which indicates either a square planar or five-coordinate pyramidal nickel center geometry (*50*). The peak areas of the 1s → 3d transition (Table 4) lie on the line between four-coordinate planar species (0−0.04 eV) and five-coordinate pyramidal species (0.04−0.09 eV) and indicate the sites that are most likely distorted four-coordinate planar in nature, consistent with what was previously reported for native *Streptomyces seoulensis* reduced NiSOD (*47*). The edge energies observed for the reduced species compare well with those of the native *S. seoulensis* enzyme.

EXAFS. The EXAFS (extended X-ray absorption fine structure) region of the XAS spectrum provides information regarding the type of scattering atoms present and their distance from the central metal ion. Table 5 and Figure 2 compare the best fits obtained for WT-NiSOD and mutant

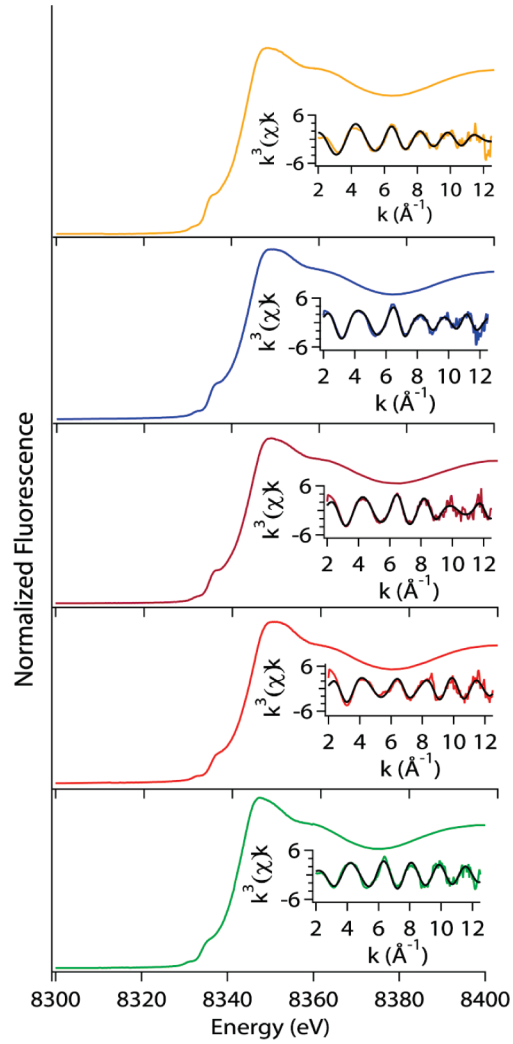

FIGURE 2: Comparison of XAS data for tyrosine mutant NiSODs: WT (yellow), Y9F (blue), Y62F (purple), Y9F/Y62F (red), and D3A (green). The main panels show normalized XANES spectra. The insets show unfiltered EXAFS data in solid colored lines and fits (black) from Table 5. The range of the *k* space fits is 2−12.5 Å^{-1} for all data.

Table 6: Redox Potentials

sample	$E°$ (mV) (vs NHE)	A_{ox}	A_{red}	N^a
WT, reduction	290(4)	0.76(1)	0.19(1)	1
WT, oxidation	279(6)	0.91(2)	0.16(5)	1
D3A, reduction	308(3)	0.815(9)	0.24(1)	1
D3A, oxidation	290(7)	0.91(3)	0.16(6)	1
Y9F, reduction	297(5)	0.54(2)	0.15(2)	1
Y9F, oxidation	299(8)	1.12(9)	0.06(6)	1

[a] *N* is the number of electrons per Ni(III) center. This value was held constant in fitting the absorption data to obtain $E°$.

NiSODs. To evaluate the change in fitting method, we collected data for reduced WT-NiSOD and compared them to previously published data (*47*). The fit is quite similar except that the Ni−N bond length is ∼0.08 Å shorter than previously found. However, prior model studies indicate that it can be difficult to obtain a distance with low error for N-scattering atoms in a complex where the EXAFS is dominated by scattering from S atoms (*50*). The new fits include atoms in the second coordination sphere, which are main chain carbon atoms from His1 and Cys2 as well as the β-carbon from Cys2 as seen in the two crystal structures of NiSOD (*17, 21*). These atoms are rigidly positioned by

chelate rings, and their inclusion improves the fits. The single mutation, Y9F-NiSOD, alters the structure around the Ni center. The best fit for Y9F-NiSOD contains two shells of sulfur donors at different distances. The first sulfur donor lies at 2.23 Å, while the other sulfur ligand is longer and lies at 2.52 Å. This splitting of the two sulfur ligands into two distances is also seen in the double mutation Y9F/Y62F-NiSOD, which has a fit similar to that of Y9F-NiSOD (Table 5). D3A- and Y62F-NiSOD have fits that are more similar to that of WT-NiSOD with both S donors at the same Ni−S distance. For D3A-NiSOD, the Ni−S bond distance found was similar to that in WT-NiSOD (0.03 Å shorter), where Y62F-NiSOD had a slightly longer Ni−S bond (0.07 Å) than WT-NiSOD (Table 5). The WT- and D3A-NiSOD fits differ by the addition of one Ni−N vector in the D3A-NiSOD fit, and the Ni−N bonds are longer in D3A-NiSOD [2.08(2) Å vs 1.83(4) Å in WT-NiSOD]. The fit obtained for Y62F-NiSOD is slightly different in that the best fit splits the two nitrogen scatterers into different shells with one ligand at 1.90 Å and the other at 2.2 Å.

The data indicate that when Tyr9 is altered by loss of the OH group, different Ni−S distances are obtained. This structural perturbation is confirmed by single-crystal diffraction studies (vide infra) and may result from the alteration of a H-bonding network in the Ni hook domain. Alternatively, the results may indicate that the nickel site is a mixture of low- and high-spin Ni centers, given the similarity of the two distances to low-spin (*51*) and high spin (*50, 51*) nickel thiolate model complexes.

PROTEIN STRUCTURE

NiSOD Crystallographic Results. The crystal structures of two NiSOD mutants, Y9F and D3A, were determined to 1.9 Å. Both the Y9F- and D3A-NiSOD mutant structures are present as hexamers with a trimer in the crystallographic asymmetric unit. In an effort to understand the structure and function of NiSOD, the structures of Y9F- and D3A-NiSOD were compared to WT-NiSOD, including both the holo and apo forms (PDB entries 1T6U, 1T6I, and 1T6Q).

Y9F Crystal Structure. The Y9F crystal structure revealed the presence of an anion-binding site near the active site in NiSOD. The WT-NiSOD structure showed the presence of two water molecules making hydrogen bonds to the hydroxyl of the Tyr9 side chain (*17*). In our Y9F-NiSOD mutant, electron density appears at locations similar to those of two water molecules in the WT-NiSOD structure. During the initial interpretation of the electron density, water molecules were placed at these locations in the structure. However, when a water molecule was refined in one of these locations, $F_o - F_c$ electron density maps showed residual electron density and positive peaks. When that water molecule was replaced with a chloride ion, the refinement then led to lower R_{free} values and the positive peak in the $F_o - F_c$ map disappeared. The location of the chloride ion is ideally suited to anion binding, with the main chain amide nitrogen atoms of residues 3, 6, and 7 pointing toward the chloride and <4 Å away.

To confirm the identity of the chloride and to probe the specificity of the putative anion-binding pocket, chloride was substituted with bromide in the crystallization of Y9F-NiSOD. Diffraction data were collected above the bromine absorption edge energy from crystals of both bromide and chloride containing Y9F-NiSOD [NiSOD (Br) and NiSOD (Cl), respectively]. The anomalous difference electron density maps from NiSOD (Br) diffraction data revealed strong density (more than eight standard deviations) in the anion-binding site, unambiguously identifying the bromide ion. In the NiSOD (Cl) crystals, no peak appeared at this location, as chloride has a negligible anomalous signal at this energy. As an internal control, the nickel ion appears in both anomalous maps, because nickel has a slight anomalous contribution (∼2 e^- vs ∼4 e^- for bromine) at this energy. To test if the anion-binding site is a feature of the Y9F structure alone, the same location in the WT-NiSOD structure was examined. Intriguingly, the coordinates of WT-NiSOD contain a water molecule at this position, but $F_o - F_c$ maps from those diffraction data show a positive peak, suggesting that the wild-type crystals may also contain some amount of chloride ion in the anion-binding pocket (Figure 3).

D3A Crystal Structure. The D3A mutation leads to the loss of two ion pairs across the interface between neighboring molecules in the hexamer. As a result, 12 ionic interactions are lost when comparing the WT structure to the D3A mutant, providing a plausible explanation for the lower thermal stability of the D3A mutant protein. The carboxyl group of Asp3 lost upon mutation to Ala leads to the loss of a salt bridge between Asp3 of one chain and Lys89 of a neighboring chain. The loss of the carboxyl group from the side chain of residue 3 produces a gap in the interface between monomers, allowing the Nζ atom of Lys89 to move toward Ala3 ∼2.0 Å to fill the space. Lys89 is critical to the network of salt bridges across the interface between monomers in the hexamer. The movement of the Lys89 side chain causes the neighboring Glu49 side chain to move by ∼2.0 Å toward Lys89. This movement of Glu49 weakens the ionic interaction between Glu49 and His53 across the interface between monomers. Therefore, mutating Asp3 to Ala results in the loss of two ionic interactions across each interchain interface (Asp3−Lys89 and Glu49−His53). With six of these interfaces in the hexamer, the loss of 12 ion pairs per hexamer could account for the decrease in the melting temperature of the mutant from 84.8 to 73.9 °C.

As a result of the disruption in the intersubunit salt bridges in the D3A structure, the "nickel hook" region is subtly perturbed. Most notably, Tyr9 has moved ∼1 Å closer to the nickel (Tyr9-O-Ni; WT-NiSOD distance of 5.47 Å; D3A-NiSOD distance of 4.26 Å), and a water molecule (W1) has been displaced from the anion-binding pocket (Figure 4).

Redox Chemistry. EPR and MCD spectroscopic methods have been used to demonstrate that the nickel centers in the resting oxidized and reduced proteins are low-spin Ni(III) and diamagnetic Ni(II) centers, respectively (*25*). We have used potentiometric titrations monitoring the absorbance at 380 nm assigned to a CysS → Ni LMCT transition in the Ni(III) complex (*25*) to measure the potential of this redox process (Figure 5). Using samples that were preoxidized with $KMnO_4$, the data from the initial reductive titrations were fit to eq 4 to yield values of $E°$ that are listed in Table 6. Reoxidation of the reduced protein with $KMnO_4$ shows that the process is reversible. The potentials obtained from fitting the oxiditative titrations are within experimental error of those obtained from the reductive titrations (Table 6). The slight increase in absorbance in the reoxidized enzyme likely

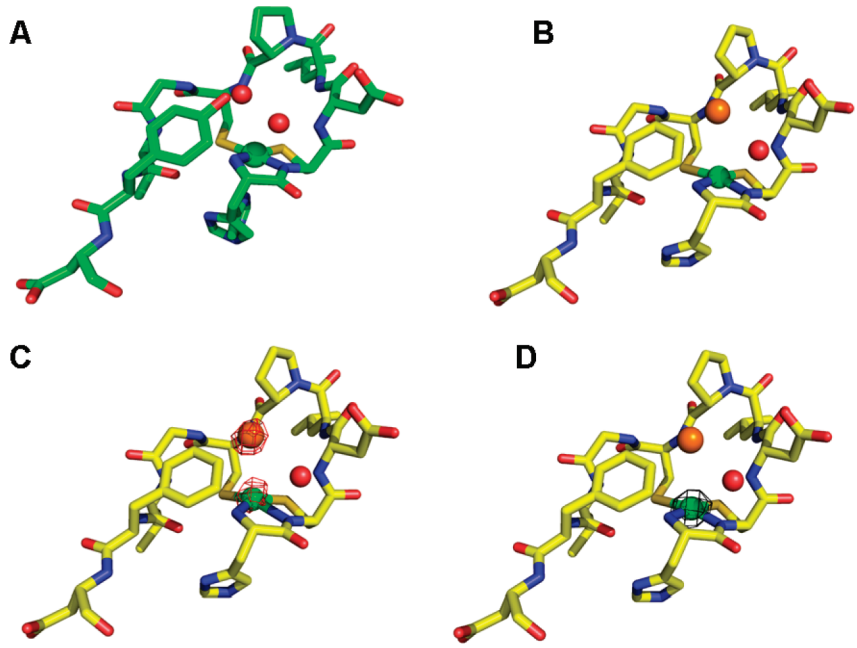

FIGURE 3: NiSOD hook domain. (A) WT-NiSOD N-terminal region showing the active site Ni ion (green sphere) and two water molecules (red spheres). (B) Same region of the Y9F-NiSOD mutant. A chloride ion (orange sphere) at the anion-binding site replaces a water molecule. (C) Same region of the Y9F-NiSOD (Br) structure. An anomalous difference map (red cage), contoured at 4σ, from data measured above the bromide absorption edge energy. Only the bromide and nickel show an anomalous signal. (D) Same region of the Y9F-NiSOD (Cl) structure. An anomalous difference map (black cage), contoured at 4σ, from data measured above the bromide absorption edge. Only the nickel shows an anomalous signal. The Ni centers are modeled as the His-off state; the actual state is most likely a mixture of His-on and His-off, but higher *B*-factors led to poorly resolved electron density at the N-terminus. Images were generated in PyMOL (*75*).

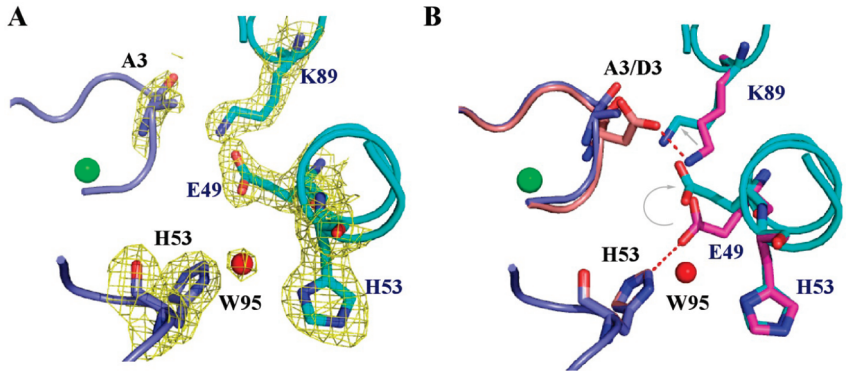

FIGURE 4: Salt bridge changes in the D3A-NiSOD mutant. (A) The D3A-NiSOD mutant is shown at the interface between neighboring monomers (blue and cyan) in the hexamer. A weighted $2F_o - F_c$ map shows the electron density in the interface. (B) Superposition of this interface from D3A-NiSOD (blue and cyan) onto the wild type (pink and magenta) shows the movement of Glu49 and Lys89. Images were generated with PyMOL (*75*).

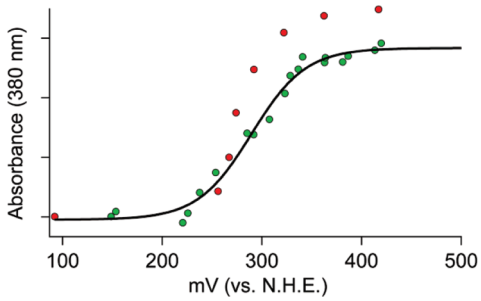

FIGURE 5: Redox titrations of WT-NiSOD. The green points are the initial reduction of oxidized to reduced NiSOD, and the red points were obtained by reoxidation of the same sample. The black line depicts the best fit of the reductive titration (green dots) using eq 4.

reflects a small concentration of the protein due to solvent loss during the long incubation under Ar that was required to stabilize the potential at each point (ca. 30 min per point). The $E°$ value obtained for WT-NiSOD [290(4) mV vs NHE] is approximately midway between the potentials for the oxidation of O_2^- to O_2.

These values are quite similar to the potentials obtained from other SODs (see Discussion). The potentials obtained for the Y9F- and D3A-NiSOD mutants are very similar to the potential of WT-NiSOD, consistent with the high catalytic rates observed for these mutants (vide infra). This result is similar to that found for MnSOD, where mutation of Tyr34 does not affect the redox potential of the Mn center (*52*).

Kinetics. The rate of dismutation of superoxide by NiSOD was determined by monitoring the decrease in the absorbance of the superoxide anion at 260 nm (ε = 2000 M^{-1} cm^{-1}) (*53*) generated by pulse radiolysis. Table 3 shows the calculated catalytic rate constant for the different tyrosine mutants of NiSOD as compared to WT. Y9F-NiSOD exhibits a slightly perturbed value of k_{calc} that is ~63% of the activity

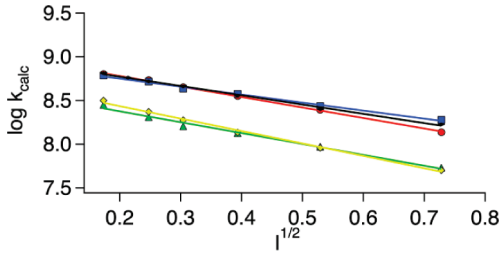

FIGURE 6: Ionic strength dependence of NiSOD catalysis. Y9F- and WT-NiSOD were reacted with both NaCl (red for WT and yellow for Y9F) and $NaClO_4$ (blue for WT and green for Y9F), while Y62F was reacted with only NaCl (black). Pulse radiolytic conditions were the same as those mentioned in Experimental Procedures, except 0.5−0.0156 M NaCl or $NaClO_4$ was added to the solution being monitored to probe the effect of ionic strength.

of WT-NiSOD. This value is slightly lower than the value obtained from *S. seoulensis* Y9F-NiSOD (*21*) (78%) using a construct in which the SOD from *Streptomyces lividans* was knocked out and replaced with a mutated copy of *S. seoulensis* (*21*). The SOD activity in that study was measured by the standard cytochrome *c* assay in cell extract (*21*). However, the studies presented here reveal that at high substrate concentrations (above a 5-fold excess), Y9F-NiSOD begins to exhibit saturation behavior. The disappearance of the absorbance at 260 nm at high superoxide concentrations relative to the enzyme concentration no longer fits a first-order process and begins to exhibit a linear component suggesting saturation behavior. The half-life for superoxide disappearance at high substrate concentrations in the presence of Y9F-NiSOD is lowered to ~41% of that in the presence of lower superoxide concentrations. Saturation kinetics is not a feature of WT-NiSOD, which cannot be saturated under these conditions. Saturation behavior is seen in MnSODs, although in that case for both the WT and mutants (*54, 55*).

The other Tyr mutant, Y62F-NiSOD, has a catalytic rate similar to that of WT-NiSOD and does not saturate, demonstrating that this residue is not intimately involved in the redox mechanism of NiSOD. This is not surprising as Tyr62 sits approximately 13 Å from the Ni center (*17, 21*). The double mutant, Y9F/Y62F-NiSOD, is generally similar to the Y9F mutant (k_{calc} ~ 35% of that of WT) and displays evidence of saturation at high substrate concentrations, consistent with the mutation at Tyr9.

The crystal structure of Y9F-NiSOD (vide supra) shows that one of the water molecules found in the active site pocket near the metal site of WT-NiSOD has been replaced with a small anion (Cl^- or Br^-) from the buffer solution. Mutation of Tyr9 may lead to an opening of the binding pocket, which would allow small anions to compete for the binding site, placing a negative charge in the path of the negatively charged superoxide and leading to diminished catalytic rates or a modification of the electrostatic component of the rate constant. To test this hypothesis, ionic strength measurements were carried out using Cl^- and ClO_4^-. Figure 6 shows a plot of the log of the calculated rate versus the square root of the ionic strength for WT, Y9F, and Y62F. The results are similar to those found for native NiSOD from *S. seoulensis* (*47*) and do not show a change from WT-NiSOD behavior as the ionic strength increases. These results suggest that small anions are not competing with superoxide during catalysis for the binding site.

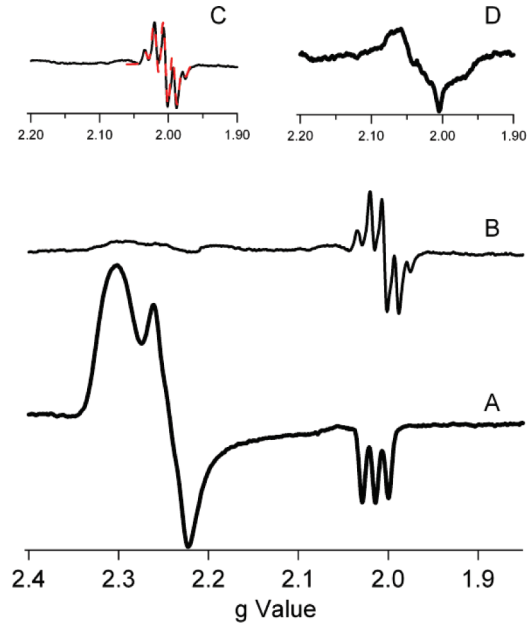

FIGURE 7: X-Band EPR data from D3A-NiSOD. (A) As-isolated D3A. (B) H_2O_2-treated D3A. (C) Enlargement of the region near $g = 2.00$ expanded (solid line) and a simulation with parameters $g_x = g_y = g_z = 2.004$, $A_{xx} = A_{yy} = 5$ G, and $A_{zz} = 20$ G (red dashed line). (D) H_2O_2-treated D3A-NiSOD (d_4-Tyr), showing alteration of hyperfine splitting due to tyrosine ring protons. All spectra are shown with the same intensity scale with the exception of panel D, which has a scale half as large.

Mutation of Asp3 to Ala results in a 50% decrease in activity at pH 7.5 when compared to that of WT-NiSOD. Upon further investigation, it was also determined that D3A-NiSOD was much more sensitive to peroxide than WT-NiSOD. To examine the nature of this sensitivity, both D3A- and WT-NiSOD were incubated with H_2O_2 for 5 min, and then the reductant or inhibitor was dialyzed away. These samples were then tested for SOD activity using pulse radiolytic generation of O_2^-. WT-NiSOD retained full activity, whereas the activity of D3A-NiSOD was below the detectable limit (data not shown). ESI-MS of D3A-NiSOD before and after H_2O_2 incubation were identical (Supporting Information), ruling out the possibility that the peroxide was causing an oxidative modification of the protein, such as conversion of the cysteine thiolate ligands to sulfinates (*24*), which would likely result in a loss of activity. However, incubation of D3A-NiSOD with peroxide did result in the production of a tyrosyl radical EPR signal (vide infra), an oxidative modification that does not affect the MW of the enzyme.

As isolated, D3A-NiSOD has the same EPR parameters as WT-NiSOD (Table 3). However, when treated with H_2O_2 [a reductant and inhibitor of NiSOD (*56*)] under anaerobic conditions, a signal attributable to a protein-based radical at $g = 2.004$ emerges with a ^1H hyperfine splitting pattern that resembles a tyrosine radical (Figure 7) (*57*). Integration of this signal versus Ni(PDTC) showed that ~8% of the enzyme possessed the tyrosine radical. This assignment was confirmed by replacing all four tyrosine residues with d_4-tyrosine, where the protons on the aromatic ring are substituted with deuterons. The resulting hyperfine splitting is clearly altered, consistent with the assignment of the hyperfine to a tyrosyl radical. (The deuterated sample is ~50% less concentrated than the nondeuterated sample.) This signal is not observed

to any significant extent in WT-NiSOD or any of the other mutants and indicates that the interaction of the enzyme with peroxide is fundamentally altered by the D3A mutation.

DISCUSSION

Redox Chemistry of the Nickel Site. The protein environments of the catalytic metal sites in SODs are responsible for achieving at least three features of these enzymes: adjusting the redox potential of the metal to a value that is optimum for catalysis (ca. 300 mV) (*8*), controlling anion access to the active site (*27*), and providing a source of protons for formation of H_2O_2 (*17, 21*). The O_2/O_2^- reduction potential has been determined to be −160 mV (vs NHE), and the O_2^-/H_2O_2 potential lies at 870 mV (vs NHE) (*58*). The midpoint of these two potentials (365 mV vs NHE) is the potential at which an optimal SOD catalyst would lie. Nickel is an unusual choice of metal for an SOD because the reduction potential of Ni_{aq}(III)/(II) is ≥2 V [1.94 V for low-spin Ni(III) and 2.24 for high-spin Ni(III)] (*6*) and lies well outside the biologically relevant range. Nonetheless, the redox titrations of NiSOD presented above establish that the redox potential of the nickel site is ∼290 mV, appropriate for SOD catalysis. The other classes of SODs (Cu/Zn, Mn, and Fe) all have reduction potentials near 300 mV (vs NHE) with deviations up to ∼100 mV (*59*−*63*). This demonstrates that the protein environment is critical for tuning the reduction potential of each metal to the optimal potential for SOD catalysis. The reduction potential for hexa-aqua complexes of Mn (1.5 V) and Fe (0.77 V) (*8, 64*) requires a smaller adjustment by the protein than Ni does. The suppression of the E_m in Mn- and FeSOD is achieved by a hydrogen bonding network that couples the protonation state of an aqua ligand to the redox process of the metal (*8*). In the case of NiSOD, no aqua ligand exists in any crystal structure, and thus, the protonation state of such a ligand is not available for adjusting the redox potential of Ni(III)/(II). Furthermore, the shift in potential for the Fe(III)/(II) redox couple in FeSOD has been attributed to the protonation state of the aqua/hydroxo ligand (*65*); such a shift would not be adequate for optimizing the potential of a nickel center in a similar ligand environment. Instead, NiSOD relies on a different ligand environment, one that includes cysteine ligands, a feature of every redox active nickel enzyme that utilizes the Ni(III)/(II) redox couple (*66*). Thus, NiSOD uses a unique strategy to accomplish the same goal, a ∼300 mV redox potential, that is found in every other SOD.

EPR integration of the Ni(III) signals in the resting, oxidized enzyme accounts for only 50% of the Ni present in WT-NiSOD and in the mutant enzymes, indicating that NiSOD contains a 50:50 mixture of Ni(II) and Ni(III). The amount of Ni present in NiSOD was determined by ICP-OES (see Experimental Procedures) after extensive buffer exchanging and treatment with Chelex to remove any nonspecifically bound metal. EXAFS analysis confirms that all of the Ni is bound in the active site, since each Ni center has two S donor ligands, and there are only two cysteine residues in the protein. Oxidation of resting, oxidized WT-NiSOD with $KMnO_4$ failed to increase the intensity of the EPR signal arising from the five-coordinate Ni(III) center (Supporting Information), indicating that the 50:50 mixture is, in fact, the fully oxidized enzyme. Although these data do not show why one nickel center is redox active and the other one is not, a likely possibility is that the apical His1 imidazole ligand plays a role. The two nickel centers differ by coordination of the imidazole ligand (His-on vs His-off), and it seems likely that the Ni(II/III) redox potential of the four-coordinate planar center is much higher than for the five-coordinate complex. In this regard, it is noteworthy that mutation of the apical His ligand to Gln (*49*) or Ala (*67*) yields mutants that have a resting oxidation state that contains only EPR-silent Ni(II). Other than a possible role in maintaining charge neutrality in the hexamer during catalysis, the biochemical rationale for the equal mix of the two oxidation states remains to be elucidated but would seem to require some cooperativity between active site centers to maintain the equal balance of oxidized and reduced nickel ions. Until now, the mechanism of communication between active sites within the hexamer that are spaced ∼25 Å apart has not been clear, but the structure of D3A-NiSOD suggests a mode for maintaining the redox balance. As described above, a network of ion pairs connect Asp3 to Lys89 to Glu49 to His53 across the interface between neighboring monomers (Figure 4) derived from different trimer subunits. His53 also lies near a 2-fold symmetry axis of the hexamer (which contains 32-point symmetry). The Nδ atom of His53 hydrogen bonds to a water molecule that lies directly on the molecular 2-fold axis. Thus, the His53 side chains from two monomers related by a molecular dyad make a water-mediated hydrogen bond, raising the possibility that information about one active site nickel may be communicated to a neighboring active site nickel.

Human MnSOD (hMnSOD) is a homotetramer and forms a dimer of dimers. A recent study examined the H-bonding network between Glu162 and His163 (a metal ligand) by mutating Glu162 to both an Ala and Asp. This H-bonding network connects neighboring monomers across a dimer interface and links two Mn centers (*54*). Both mutations retained tetrameric structure and specificity for Mn over Fe [in contrast, studies of the analogous mutation made in *E. coli* MnSOD (*Ec*MnSOD), a homodimer, show the mutant enzyme preferred Fe over Mn (*55*)]. Both the human Glu162 mutations have diminished activity compared to WT-hMnSOD (*54*), but each helps to elucidate fine points of how hMnSOD carries out O_2^- dismutation. By performing pH titrations on the enzyme and monitoring the electronic absorption spectrum, the pK_a of the system can be determined. WT-hMnSOD has a pK_a of ∼9.5, which has been attributed to ionization of Tyr34 (*32, 68, 69*). In the E162D-hMnSOD mutant, the pK_a decreases slightly to 8.7(2), while the E162A-hMnSOD pK_a is closer to the pK_a of Tyr in water [10.1(1)] (*54*). This can be explained by the interaction of Glu162 and Tyr34, which are 6.2 Å apart. The H-bonding network extends from the carboxylate of Glu162 to His143 through a solvent molecule to Tyr34. This network is maintained in the E162D-hMnSOD mutant but is disrupted in the E162A-hMnSOD mutant. This is analogous to the backbone amide of Asp3 in NiSOD, which is connected to the phenol proton on Tyr9 through a H-bonding network involving ordered water in the pocket. This network is perturbed in the D3A-NiSOD mutant, and perturbed kinetics and peroxide sensitivity are observed. (It is noteworthy that in hMnSOD, there is no functional difference between

E162A and E162D mutants despite the structural difference. In NiSOD, there is a functional difference.)

Roles of Tyr9 in NiSOD Catalysis. Mutations of conserved second-coordination sphere residues, Tyr9, Asp3, and the more distant Tyr62, do not lead to major perturbations of the protein structure, or of either the electronic structure or redox chemistry of the nickel site. However, both the Tyr9 and Asp3 mutations have significant effects on catalysis. In the case of Y9F, there is a small decrease in k_{calc} and the enzyme shows the onset of saturation behavior that is not a feature of WT-NiSOD under the conditions studied. In the case of D3A-NiSOD, the loss of activity is more pronounced; the enzyme is somewhat less thermally stable and exhibits distinct reactivity with H_2O_2.

The roles played by the Tyr9 residue in catalysis can account for much of the altered functions of Y9F- and D3A-NiSOD. The structure of WT-NiSOD reveals no water molecules coordinated to either the five-coordinate pyramidal His-on Ni(III) center or the reduced four-coordinate planar His-off Ni(II) center. Tyr9 lies near the vacant sixth coordination position with a Ni−O-Tyr9 distance of 5.47 Å. The position of Tyr9 is such that the phenol proton is engaged in hydrogen bonds with two ordered water molecules, W1 at 2.56 Å and W2 at 2.84 Å, that also accept hydrogen bonds from amide protons from Cys6 (W1) and Asp3 (W2) (*17, 21*). In the Y9F mutant, loss of the phenol group leads to a small perturbation in the position of the phenyl ring, opening up the existing anion binding pocket (Figure 3), and W1 is replaced with Cl^-. This is the first crystallographic characterization of an anion complex of NiSOD and clearly identifies a likely binding site for the substrate, O_2^-. That Cl^- is not a nickel ligand is evidenced by the 3.5 Å distance, the absence of a Ni−Cl vector in the EXAFS spectrum, and the lack of chlorine hyperfine splitting (even at 200 mM Cl^-) in the EPR spectrum, particularly on g_z which exhibits large N hyperfine splitting (A_z = 25 G) from the apical H1 imidazole ligand in the $d_{z^2}^1$ ground state. Hyperfine splitting from the enzyme (likely due to the amide and or N-terminal amine N-donor ligands) is partially resolved on g_y in Y9F-NiSOD. Similar hyperfine splitting on the g_y feature has also been observed in azide-inhibited NiSOD (*17*). When ^{15}N-labeled azide was used, the same EPR spectrum was observed, indicating that the splitting was due to an electronic and/or structural perturbation rather than to azide binding (*17*). Further, the Cl^- in the Y9F-NiSOD structure is in the same location that was previously suggested for azide (anion) binding (*17*). The Cl^- anion has hydrogen bonding interactions with both of the amides from Cys6 (N−Cl distance of 3.4 Å) and Asp3 (N−Cl distance of 3.4 Å), which provide a mechanism for a small perturbation of the nickel site. The Cl^- is positioned such that it could interact with the phenol group of Tyr9 in WT-NiSOD, which suggests possible roles for Tyr9 in the release of H_2O_2, and in controlling access of anions to the active site. The size of the pocket in WT-NiSOD is appropriate for only small anions and is positioned near the nickel site but does not allow anions to bind to the metal. Since there is no evidence of anion binding to Ni in either His-on [Ni(III)] or His-off [Ni(II)] sites, and assuming that O_2^- binds to the same site, the structural data support an outer-sphere redox reaction for both half-reactions as illustrated in Scheme 1.

In an outer-sphere mechanism, the superoxide would displace the two water molecules (Scheme 1, I) and sit between the backbone amides of Asp3 and Cys6 (Scheme 1, II). Electron transfer would occur, yielding molecular oxygen and Ni(II) (Scheme 1, II → III). The second half of the reaction starts the same as the first half, with superoxide binding in the substrate binding pocket (Scheme 1, IV). Electron transfer occurs concomitant with proton transfers, leading to formation of peroxide and Ni(III). Loss of the phenol group and opening of the anion-binding pocket lead to a small perturbation in the position of the phenyl ring and increased occupancy of the site by Cl^- and Br^- in the absence of O_2^- (Figure 3). When the bound peroxide is protonated, the phenol group could play a role in destabilizing the binding of the product, H_2O_2, in the anion binding site and inhibiting the direct interaction with the nickel site and its oxidation-sensitive cysteine thiolate ligands. Slower peroxide release in the absence of the phenol group could account for the decrease in activity and the saturation behavior observed in Y9F-NiSOD kinetics.

It has been shown that binding of azide to *Ec*MnSOD is temperature-dependent. At low temperatures, a six-coordinate complex derived from complexation of azide is formed, whereas at room temperature, the active site is five-coordinate and lacks an azide ligand, resembling the resting enzyme (*31, 70, 71*). One hypothesis speculates that a "dead-end" complex of *Ec*MnSOD forms when superoxide binds to Mn^{2+}-SOD, causing oxidation of the Mn center and reduction of superoxide to peroxide with concomitant transfer of a proton from the bound water to yield a Mn center with bound hydroperoxide and OH^- (*31*). The Y34F mutation changes the way the enzyme interacts with anions. When azide is added to Y34F-Mn^{3+}-SOD, the enzyme resembles the low-temperature six-coordinate N_3-Mn^{3+}-SOD complex and exhibits no temperature dependence (*71*). Thus, the "gateway" tyrosine seems to play a critical role in controlling access of anions to the metal site in both Fe- and MnSODs (*15, 16, 71*) by inhibiting anion binding at the metal center. The same function for Tyr9 appears to be a feature of NiSOD catalysis. Second-sphere residues such as Tyr34 also tune the lability of the peroxide product in MnSOD. This is seen in the fact that the activity of Y34F-MnSOD is more product-inhibited than that of WT-MnSOD (*68*).

Another possible explanation might be that mutation of Tyr9 and loss of W1 from the active site perturb a hydrogen bonding network that is important for supplying protons for the formation of H_2O_2 (*17, 21*). This has also been proposed for MnSOD, where the H-bonding network in the second coordination sphere has been implicated as the source of protons for the release of H_2O_2 (*68, 72*). Studies of Tyr34 from hMnSOD shows that replacing the Tyr with a Phe has little effect on the protein fold or the geometry at the active site; in fact, the thermal stability of the mutant is increased when compared to that of WT-hMnSOD (*68*). Tyr34 is not essential for MnSOD catalysis, as at low substrate concentrations (compared to K_m) Y34F-MnSOD has catalytic rates similar to that of WT-MnSOD. This is shown by the fact that the steady state constant, k_{cat}/K_m, is the nearly identical for both Y34F- and WT-MnSOD and is near the diffusion limit of 10^9 M^{-1} s^{-1}. The only major perturbation is the decrease in the maximal rate, k_{cat}, which is approximately 10-fold lower for the mutant enzyme (*68*). This implies that

Scheme 1: Proposed Outer-Sphere Mechanism for NiSOD[a]

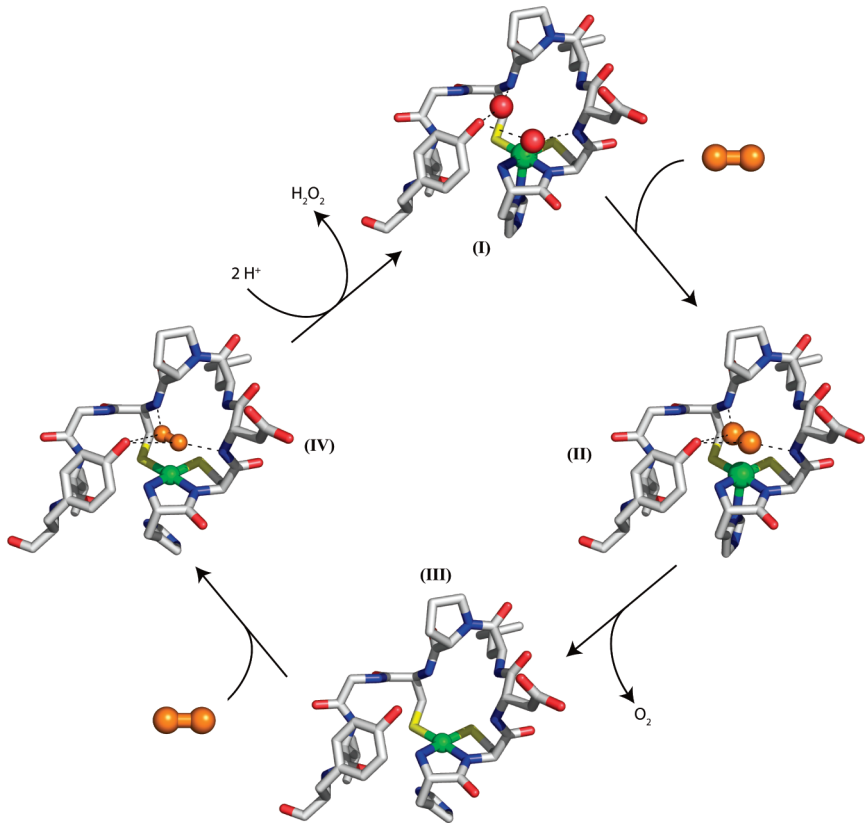

[a] Ni(III) is indicated by the His-on complex, while Ni(II) is denoted as a His-off complex, although removal of His1 during turnover may not occur. Superoxide is denoted by the orange molecule, and water is denoted by red spheres. Images were generated with PyMOL (*75*).

Tyr34 may be involved in peroxide release or proton donation either directly to the metal site or indirectly through a H-bonding network that ties the Tyr34 to the Mn active site (*68*). Mutation of Tyr34 has also been examined in FeSOD from *E. coli* (*Ec*FeSOD), and Y34F-FeSOD results in a rate decrease of ~60% when compared to that of WT-FeSOD (*33*). The gateway Tyr residue in FeSOD also seems to play a key role in controlling anion binding to the metal site, which differs between the reduced and oxidized state in FeSOD (*15*).

The importance of Tyr9 in controlling the access of H_2O_2 to the active site is supported by studies of D3A-NiSOD. Although this mutant exhibits reduced activity relative to WT-NiSOD, redox titration shows that this is not due to alteration of the redox potential of the nickel site. Further, the similar EPR spectrum obtained from Ni(III) centers in the oxidized enzyme shows that the electronic structure of the nickel site is not perturbed by the D3A mutation. Nonetheless, this mutant exhibits a drastically altered interaction with H_2O_2. Unlike WT-NiSOD, which shows inhibition (activity can be restored to normal levels upon removal of peroxide) by H_2O_2, D3A-NiSOD is inactivated (loss of activity is irreversible) by exposure to H_2O_2. This inactivation does not result from oxygenation of the cysteine residues but appears to involve the oxidation of Tyr9 to a tyrosyl radical as detected by EPR. The crystal structure of D3A-NiSOD reveals that in addition to the loss of two intersubunit interactions per monomer resulting in a hexamer with lower thermal stability, the position of Tyr9 is altered. In D3A-NiSOD, the tyrosine is positioned such that the phenol group

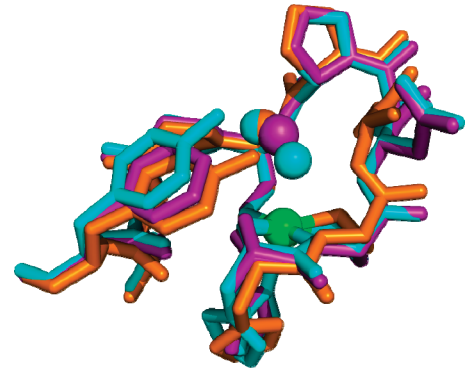

FIGURE 8: Superposition of the Ni hook domains of WT-NiSOD (blue), Y9F-NiSOD (purple), and D3A-NiSOD (orange) showing the position of Y9 in each. This image was generated with PyMOL (*75*).

is ~1 Å closer to the nickel site (Figure 8). In this configuration, it is in a position that would be less effective in inhibiting access of H_2O_2 to the nickel site and could even stabilize formation of a Ni-OOH peroxo or superoxo adduct that results in oxidation of Tyr9.

Mutation of Tyr34 in MnSOD leads to a more product-inhibited form of the enzyme, which is pronounced in hMnSOD and not as evident in *E. coli* MnSOD (*Ec*MnSOD) (*73*). To probe this inhibition further, Phe66 from hMnSOD was studied because it contributes to the local environment of Tyr34 (*74*). Phe66 also lies at a dimer interface of hMnSOD, and when this was mutated to an Ala, there were no major perturbations as the enzyme acted in a manner very

similar to that of WT-hMnSOD. F66L-hMnSOD exhibited a decrease in the level of product inhibition and had characteristics similar to that of *Ec*MnSOD. Crystallographic characterization of F66L-hMnSOD has provided insight into why this particular mutant had a decreased level of product inhibition. The substitution of Phe66 with Leu had an effect on two residues. First, Gln119 moved approximately 1 Å farther from the Mn site but maintained the same distance between residues 66 and 119 as seen in WT-hMnSOD. Tyr34 also had a subtle movement of 0.3 Å away from the Mn center. This movement is small and has a high uncertainty due to the resolution of the structure (2.2 Å). This is consistent with the data presented here in that inward movement of the gateway tyrosine (Tyr9 of NiSOD and Tyr34 of MnSOD) leads to a more product sensitive enzyme. When the corresponding residue swings away from the metal center, this inhibition is attenuated in hMnSOD and is not seen in NiSOD.

The angle of the aromatic ring plane of residue 9 (Figure 8) may also act as a sensor for the presence of bound metal. When the locations of Tyr9 in the holo- and apo-NiSOD structures are compared, the angle of the residue 9 aromatic ring plane changes by 15° between the two structures. This difference is consistent in all 12 copies of the holoenzyme monomer in PDB entry 1T6U and all six copies of the apoenzyme in 1T6I and 1T6Q. Thus, the aromatic ring may also be a sensor for the presence of a metal in the active site of the enzyme. In the case of the Y9F-NiSOD mutant structure, the angle of the aromatic ring of residue 9 is more consistent with the apo structures, producing a structure intermediate between the active holoenzyme and the inactive apoenzyme. The Y9F mutant is the first structure in which the angle of the residue 9 side chain is decoupled from the presence of metal in the active site of the enzyme. This observation is consistent with the result that the Y9F mutant does not bind nickel as efficiently as the wild-type enzyme (the crystals have only 60% occupancy). Additionally, the eight N-terminal residues that comprise the Ni hook domain have higher *B*-factors and lower quality density than the rest of the structure, suggesting some heterogeneity in the region around the Ni center. It appears that the Ni is required to properly form a well-ordered static Ni hook region at the N-terminus.

Structural Homology between MnSOD and NiSOD. The analogous functional roles ascribed to Tyr9 in NiSOD and Tyr34 in MnSOD are also reflected in their structural relationship with their respective metal centers. Both tyrosine phenol oxygen atoms lie at a M−O distance of ca. 5.5 Å and are engaged in well-defined hydrogen bonding interactions. In addition, both are close to a second aromatic residue. In the case of MnSOD, Tyr34 lies between Phe66 and the manganese center. The F66L-MnSOD mutation in hMnSOD results in perturbation of the positions of water molecules and hydrogen bonding interactions that leads to a mutant enzyme that is less sensitive to peroxide inhibition (*74*). In WT-NiSOD, Tyr62 lies ~13 Å from the nickel center and Tyr9 lies between it and the metal. Neither the structure of the nickel site (XAS and EPR) nor the kinetic properties of Y62F-NiSOD differ from significantly from those of WT-NiSOD. Although no similar function has been found for NiSOD Tyr62 and human MnSOD Phe66, they share the same spatial relationship to the respective Tyr residues near the metal sites. This is clearly shown in Figure 9, which shows a superposition of the active site of the human MnSOD structure (PDB entry 1LUV) and WT-NiSOD (PDB entry 1T6U), where Phe66 from MnSOD and Tyr62 from NiSOD were constrained to overlap. Thus, it can be seen that despite the lack of any primary, secondary, tertiary, or quaternary structure, the two enzymes have arrived at the same mechanism for controlling access of anions and H_2O_2 to the active site.

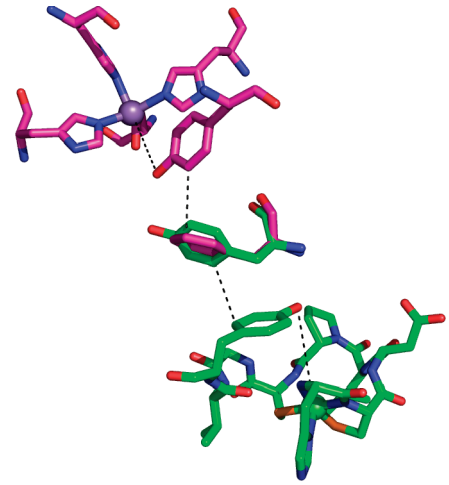

FIGURE 9: Superposition of the active site structures of hMnSOD (pink) and *S. coelicolor* NiSOD (green) showing the positions of aromatic residues. This image was generated with PyMOL (*75*).

SUPPORTING INFORMATION AVAILABLE

Amino acid sequence alignments for selected NiSODs, DSC thermograms, ESI-MS under nondenaturing conditions, EPR spectra of WT-NiSOD and mutant NiSODs and as-isolated and $KMnO_4$-oxidized WT-NiSOD, and tables of EXAFS fits. This material is available free of charge via the Internet at http://pubs.acs.org.

REFERENCES

1. Cabelli, D. E., Riley, D., Rodriguez, J. A., Valentine, J. S., and Zhu, H. (1998) Models of Superoxide Dismutases. In *Biomimetic Oxidations Catalyzed by Transition Metal Complexes* (Meunier, B., Ed.) Chapter 10.
2. Fridovich, I. (1995) Superoxide radical and superoxide dismutases. *Annu. Rev. Biochem. 64*, 97–112.
3. Miller, A. F., and Sorkin, D. (1997) Superoxide Dismutases: A Molecular Perspective. *Comments Mol. Cell. Biophys. 9*, 1–48.
4. Touati, D. (1997) Superoxide Dismutases in Bacteria and Pathogen Protists. In *Oxidative Stress and the Molecular Biology of Antioxidant Defenses* (Scandalios, J. G., Ed.) pp 447−493, Cold Spring Harbor Laboratory Press, Plainview, NY.
5. Lee, J. W., Roe, J. H., and Kang, S. O. (2002) Nickel-containing superoxide dismutase. In *Superoxide Dismutase*, pp 90−101.
6. Uudsemaa, M., and Tamm, T. (2003) Density-functional theory calculations of aqueous redox potentials of fourth-period transition metals. *J. Phys. Chem. A 107*, 9997–10003.
7. Jackson, T. A., and Brunold, T. C. (2004) Combined spectroscopic/computational studies on Fe- and Mn-dependent superoxide dismutases: Insights into second-sphere tuning of active site properties. *Acc. Chem. Res. 37*, 461–470.
8. Miller, A. F. (2008) Redox tuning over almost 1 V in a structurally conserved active site: Lessons from Fe-containing superoxide dismutase. *Acc. Chem. Res. 41*, 501–510.
9. Vance, C. K., and Miller, A. F. (1998) Simple proposal that can explain the inactivity of metal-substituted superoxide dismutases. *J. Am. Chem. Soc. 120*, 461–467.

10. Rulisek, L., Jensen, K. P., Lundgren, K., and Ryde, U. (2006) The reaction mechanism of iron and manganese superoxide dismutases studied by theoretical calculations. *J. Comput. Chem. 27*, 1398–1414.
11. Carrasco, R., Morgenstern-Badarau, I., and Cano, J. (2007) Two proton-one electron coupled transfer in iron and manganese superoxide dismutases: A density functional study. *Inorg. Chim. Acta 360*, 91–101.
12. Miller, A. F., Padmakumar, K., Sorkin, D. L., Karapetian, A., and Vance, C. K. (2003) Proton-coupled electron transfer in Fe-superoxide dismutase and Mn-superoxide dismutase. *J. Inorg. Biochem. 93*, 71–83.
13. Fisher, C. L., Cabelli, D. E., Hallewell, R. A., Beroza, P., Lo, T. P., Getzoff, E. D., and Tainer, J. A. (1997) Computational, pulse-radiolytic, and structural investigations of lysine-136 and its role in the electrostatic triad of human Cu,Zn superoxide dismutase. *Proteins: Struct., Funct., Genet. 29*, 103–112.
14. Vance, C. K., and Miller, A. F. (1998) Spectroscopic comparisons of the pH dependencies of Fe-substituted (Mn)superoxide dismutase and Fe-superoxide dismutase. *Biochemistry 37*, 5518–5527.
15. Miller, A. F., Sorkin, D. L., and Padmakumar, K. (2005) Anion binding properties of reduced and oxidized iron-containing superoxide dismutase reveal no requirement for tyrosine 34. *Biochemistry 44*, 5969–5981.
16. Tabares, L. C., Cortez, N., and Un, S. (2007) Role of tyrosine-34 in the anion binding equilibria in manganese(II) superoxide dismutases. *Biochemistry 46*, 9320–9327.
17. Barondeau, D. P., Kassmann, C. J., Bruns, C. K., Tainer, J. A., and ansd Getzoff, E. D. (2004) Nickel Superoxide Dismutase Structure and Mechanism. *Biochemistry 43*, 8038–8047.
18. Borgstahl, G. E. O., Pokross, M., Chehab, R., Sekher, A., and Snell, E. H. (2000) Cryo-trapping the six-coordinate, distorted-octahedral active site of manganese superoxide dismutase. *J. Mol. Biol. 296*, 951–959.
19. Kerfeld, C. A., Yoshida, S., Tran, K. T., Yeates, T. O., Cascio, D., Bottin, H., Berthomieu, C., Sugiura, M., and Boussac, A. (2003) The 1.6 angstrom resolution structure of Fe-superoxide dismutase from the thermophilic cyanobacterium *Thermosynechococcus elongatus*. *J. Biol. Inorg. Chem. 8*, 707–714.
20. Strange, R. W., Antonyuk, S., Hough, M. A., Doucette, P. A., Rodriguez, J. A., Hart, P. J., Hayward, L. J., Valentine, J. S., and Hasnain, S. S. (2003) The structure of holo and metal-deficient wild-type human Cu, Zn superoxide dismutase and its relevance to familial amyotrophic lateral sclerosis. *J. Mol. Biol. 328*, 877–891.
21. Wuerges, J., Lee, J. W., Yim, Y. I., Yim, H. S., Kang, S. O., and Carugo, K. D. (2004) Crystal structure of nickel-containing superoxide dismutase reveals another type of active site. *Proc. Natl. Acad. Sci. U.S.A. 101*, 8569–8574.
22. Chohan, B. S., and Maroney, M. J. (2006) Selective oxidations of a dithiolate complex produce a mixed sulfonate/thiolate complex. *Inorg. Chem. 45*, 1906–1908.
23. Grapperhaus, C. A., and Darensbourg, M. Y. (1998) Oxygen Capture by Sulfur in Nickel Thiolates. *Acc. Chem. Res. 31*, 451–459.
24. Kumar, M., Colpas, G. J., Day, R. O., and Maroney, M. J. (1989) Ligand Oxidation in a Nickel Thiolate Complex: A Model for the Deactivation of Hydrogenase by O_2. *J. Am. Chem. Soc. 111*, 8323–8325.
25. Fiedler, A. T., Bryngelson, P. A., Maroney, M. J., and Brunold, T. C. (2005) Spectroscopic and Computational Studies of Ni Superoxide Dismutase: Electronic Structure Contributions to Enzymatic Function. *J. Am. Chem. Soc. 127*, 5449–5462.
26. Pelmenschikov, V., and Siegbahn, P. E. M. (2006) Nickel superoxide dismutase reaction mechanism studied by hybrid density functional methods. *J. Am. Chem. Soc. 128*, 7466–7475.
27. Bertini, I., Banci, L., Piccioli, M., and Luchinat, C. (1990) Spectroscopic Studies on Cu2Zn2SOD: A Continuous Advancement of Investigation Tools. *Coord. Chem. Rev. 100*, 67–103.
28. Banci, L., Bertini, I., Cabelli, D. E., Hallewell, R. A., Luchinat, C., and Viezzoli, M. S. (1991) Advances in the understanding of the structure-function relationship in Cu,Zn superoxide dismutase. *Free Radical Res. Commun. 12−13* (Part 1), 239–251.
29. Getzoff, E. D., Cabelli, D. E., Fisher, C. L., Parge, H. E., Viezzoli, M. S., Banci, L., and Hallewell, R. A. (1992) Faster superoxide dismutase mutants designed by enhancing electrostatic guidance. *Nature 358*, 347–351.
30. Getzoff, E. D., Tainer, J. A., Weiner, P. K., Kollman, P. A., Richardson, J. S., and Richardson, D. C. (1983) Electrostatic Recognition Between Superoxide and Copper,Zinc Superoxide-Dismutase. *Nature 306*, 287–290.
31. Jackson, T. A., Karapetian, A., Miller, A. F., and Brunold, T. C. (2004) Spectroscopic and computational studies of the azide-adduct of manganese superoxide dismutase: Definitive assignment of the ligand responsible for the low-temperature thermochromism. *J. Am. Chem. Soc. 126*, 12477–12491.
32. Maliekal, J., Karapetian, A., Vance, C., Yikilmaz, E., Wu, Q., Jackson, T., Brunold, T. C., Spiro, T. G., and Miller, A. F. (2002) Comparison and contrasts between the active site PKs of Mn-superoxide dismutase and those of Fe-superoxide dismutase. *J. Am. Chem. Soc. 124*, 15064–15075.
33. Hunter, T., Ikebukuro, K., Bannister, W. H., Bannister, J. V., and Hunter, G. J. (1997) The conserved residue tyrosine 34 is essential for maximal activity of iron-superoxide dismutase from *Escherichia coli*. *Biochemistry 36*, 4925–4933.
34. Kruger, H. J., Peng, G., and Holm, R. H. (1991) Low-Potential Nickel(III,II) Complexes: New Systems Based on Tetradentate Amidate Thiolate Ligands and the Influence of Ligand Structure on Potentials in Relation to the Nickel Site in Ni,Fe-Hydrogenases. *Inorg. Chem. 30*, 734–742.
35. Reiter, T. A., and Rusnak, F. (2004) Electrochemical studies of the mono-Fe, Fe-Zn, and Fe-Fe metalloisoforms of bacteriophage lambda protein phosphatase. *Biochemistry 43*, 782–790.
36. Watanabe, T., and Honda, K. (1982) Measurement of the Extinction Coefficient of the Methyl Viologen Cation Radical and the Efficiency of Its Formation by Semiconductor Photocatalysis. *J. Phys. Chem. 86*, 2617–2619.
37. Bernhardt, P. V., Chen, K. I., and Sharpe, P. C. (2006) Transition metal complexes as mediator-titrants in protein redox potentiometry. *J. Biol. Inorg. Chem. 11*, 930–936.
38. Leitch, S., Bradley, M. J., Rowe, J. L., Chivers, P. T., and Maroney, M. J. (2007) Nickel-specific response in the transcriptional regulator *Escherichia coli* NikR. *J. Am. Chem. Soc. 129*, 5085–5095.
39. Padden, K. M., Krebs, J. F., MacBeth, C. E., Scarrow, R. C., and Borovik, A. S. (2001) Immobilized metal complexes in porous organic hosts: Development of a material for the selective and reversible binding of nitric oxide. *J. Am. Chem. Soc. 123*, 1072–1079.
40. Webb, S. M. (2005) SIXPack: A graphical user interface for XAS analysis using IFEFFIT. *Phys. Scr. T115*, 1011–1014.
41. Ankudinov, A. L., Ravel, B., Rehr, J. J., and Conradson, S. D. (1998) Real-space multiple-scattering calculation and interpretation of X-ray-absorption near-edge structure. *Phys. Rev.B 58*, 7565–7576.
42. Zabinsky, S. I., Rehr, J. J., Ankudinov, A., Albers, R. C., and Eller, M. J. (1995) Multiple-Scattering Calculations of X-ray-Absorption Spectra. *Phys. Rev. B 52*, 2995–3009.
43. Otwinowski, Z., and Minor, W. (1997) Processing of X-ray Diffraction Data Collected in Oscillation Mode. In *Methods in Enzymology: Macromolecular Crystallography, Part A* (Abelson, J. N., Simon, M. I., Jr., Carter, C. W., and Sweet, R. M., Eds.) pp 307−326, Academic Press, New York.
44. Collaborative Computational Project No. 4 (1994) The CCP4 Suite: Programs for Protein Crystallography. *Acta Crystallogr. D50*, 760–763.
45. Jones, T. A., Zou, J. Y., Cowan, S. W., and Kjeldgaard, M. (1991) Improved methods for building protein models in electron density maps and the location of errors in these models. *Acta Crystallogr. A47*, 110–119.
46. Laskowski, R. A., Macarthur, M. W., Moss, D. S., and Thornton, J. M. (1993) PROCHECK: A program to check the stereochemical quality of protein structures. *J. Appl. Crystallogr. 26*, 283–291.
47. Choudhury, S. B., Lee, J.-W., Davidson, G., Yim, Y.-I., Bose, K., Sharma, M. L., Kang, S.-O., Cabelli, D. E., and Maroney, M. J. (1999) Examination of the Nickel Site Structure and Reaction Mechanism in *Streptomyces seoulensis* Superoxide Dismutase. *Biochemistry 38*, 3744–3752.
48. Solvay Chemicals, Inc. (2004) Technical Data Sheet HH-121.
49. Bryngelson, P. A., Arobo, S. E., Pinkham, J. L., Cabelli, D. E., and Maroney, M. J. (2004) Expression, reconstitution, and mutation of recombinant *Streptomyces coelicolor* NiSOD. *J. Am. Chem. Soc. 126*, 460–461.
50. Colpas, G. J., Maroney, M. J., Bagyinka, C., Kumar, M., Willis, W. S., Suib, S. L., Baidya, N., and Mascharak, P. K. (1991) X-ray Spectroscopic Studies of Nickel-Complexes, with Application to the Structure of Nickel Sites in Hydrogenases. *Inorg. Chem. 30*, 920–928.

51. Colpas, G. J., Kumar, M., Day, R. O., and Maroney, M. J. (1990) Structural Investigations of Nickel Complexes with Nitrogen and Sulfur Donor Ligands. *Inorg. Chem. 29*, 4779–4788.
52. Leveque, V. J., Vance, C. K., Nick, H. S., and Silverman, D. N. (2001) Redox properties of human manganese superoxide dismutase and active-site mutants. *Biochemistry 40*, 10586–10591.
53. Rabani, J., and Nielsen, S. O. (1969) Absorption Spectrum and Decay Kinetics of O_2^- and HO_2 in Aqueous Solutions by Pulse Radiolysis. *J. Phys. Chem. 73*, 3736.
54. Quint, P. S., Domsic, J. F., Cabelli, D. E., McKenna, R., and Silverman, D. N. (2008) Role of a glutamate bridge spanning the dimeric interface of human manganese superoxide dismutase. *Biochemistry 47*, 4621–4628.
55. Whittaker, M. M., and Whittaker, J. W. (1998) A glutamate bridge is essential for dimer stability and metal selectivity in manganese superoxide dismutase. *J. Biol. Chem. 273*, 22188–22193.
56. Szilagyi, R. K., Bryngelson, P. A., Maroney, M. J., Hedman, B., Hodgson, K. O., and Solomon, E. I. (2004) S K-edge X-ray absorption spectroscopic investigation of the Ni-containing superoxide dismutase active site: New structural insight into the mechanism. *J. Am. Chem. Soc. 126*, 3018–3019.
57. Barry, B. A., and Einarsdottir, O. (2005) Insights into the structure and function of redox-active tyrosines from model compounds. *J. Phys. Chem. B 109*, 6972–6981.
58. Fee, J. A., and Valentine, J. S. (1977) Chemistry of O_2^-. In *Superoxide and superoxide dismutases* (Michelson, A. M., McCord, J. M., and Fridovich, I., Ed.) pp 25−28, Academic Press, New York.
59. Ge, B., Scheller, F. W., and Lisdat, F. (2003) Electrochemistry of immobilized CuZnSOD and FeSOD and their interaction with superoxide radicals. *Biosensors Bioelectronics 18*, 295–302.
60. Leveque, V. J. P., Vance, C. K., Nick, H. S., and Silverman, D. N. (2001) Redox properties of human manganese superoxide dismutase and active-site mutants. *Biochemistry 40*, 10586–10591.
61. St. Clair, C. S., Gray, H. B., and Valentine, J. S. (1992) Spectroelectrochemistry of Copper-Zinc Superoxide-Dismutase. *Inorg. Chem. 31*, 925–927.
62. Vance, C. K., and Miller, A. F. (2001) Novel insights into the basis for *Escherichia coli* superoxide dismutase's metal ion specificity from Mn-substituted FeSOD and its very high E-m. *Biochemistry 40*, 13079–13087.
63. Barrette, W. C., Jr., Sawyer, D. T., Fee, J. A., and Asada, K. (1983) Potentiometric titrations and oxidation-reduction potentials of several iron superoxide dismutases. *Biochemistry 22*, 624–627.
64. Lange, N. A., and Dean, J. A. (1985) *Lange's Handbook of Chemistry*, 13th ed., McGraw-Hill, New York.
65. Yikilmaz, E., Porta, J., Grove, L. E., Vahedi-Faridi, A., Bronshteyn, Y., Brunold, T. C., Borgstahl, G. E., and Miller, A. F. (2007) How can a single second sphere amino acid substitution cause reduction midpoint potential changes of hundreds of millivolts? *J. Am. Chem. Soc. 129*, 9927–9940.
66. Maroney, M. J. (1999) Structure/function relationships in nickel metallobiochemistry. *Curr. Opin. Chem. Biol. 3*, 188–199.
67. Ryan, K. C., and Maroney, M. J. Unpublished results.
68. Guan, Y., Hickey, M. J., Borgstahl, G. E. O., Hallewell, R. A., Lepock, J. R., O'Connor, D., Hsieh, Y. S., Nick, H. S., Silverman, D. N., and Tainer, J. A. (1998) Crystal structure of Y34F mutant human mitochondrial manganese superoxide dismutase and the functional role of tyrosine 34. *Biochemistry 37*, 4722–4730.
69. Hsu, J. L., Hsieh, Y. S., Tu, C. K., Oconnor, D., Nick, H. S., and Silverman, D. N. (1996) Catalytic properties of human manganese superoxide dismutase. *J. Biol. Chem. 271*, 17687–17691.
70. Whittaker, M. M., and Whittaker, J. W. (1996) Low-temperature thermochromism marks a change in coordination for the metal ion in manganese superoxide dismutase. *Biochemistry 35*, 6762–6770.
71. Whittaker, M. M., and Whittaker, J. W. (1997) Mutagenesis of a proton linkage pathway in *Escherichia coli* manganese superoxide dismutase. *Biochemistry 36*, 8923–8931.
72. Edwards, R. A., Whittaker, M. M., Whittaker, J. W., Baker, E. N., and Jameson, G. B. (2001) Outer sphere mutations perturb metal reactivity in manganese superoxide dismutase. *Biochemistry 40*, 15–27.
73. Abreu, I. A., Hearn, A., An, H., Nick, H. S., Silverman, D. N., and Cabelli, D. E. (2008) The kinetic mechanism of manganese-containing superoxide dismutase from *Deinococcus radiodurans*: A specialized enzyme for the elimination of high superoxide concentrations. *Biochemistry 47*, 2350–2356.
74. Zheng, J., Domsic, J. F., Cabelli, D., McKenna, R., and Silverman, D. N. (2007) Structural and Kinetic Study of Differences between Human and *Escherichia coli* Manganese Superoxide Dismutases. *Biochemistry 46*, 14830–14837.
75. DeLano, W. L. (2002) *The PyMOL Molecular Graphics System*, DeLano Scientific, Palo Alto, CA.

BI802029T